Journal of Nanobiotechnology

RESEARCH

Open Access

A multifunctional injectable, self-healing, and adhesive hydrogel-based wound dressing stimulated diabetic wound healing with combined reactive oxygen species scavenging, hyperglycemia reducing, and bacteria-killing abilities

Rong Chen[1†], Pinkai Wang[2†], Jiajun Xie[2†], Zinan Tang[1], Jinlang Fu[1], Yanhong Ning[1], Qiang Zhong[1], Ding Wang[1], Mingyuan Lei[1], Huaming Mai[1], Hao Li[1], Zhanjun Shi[1*], Jian Wang[1*] and Hao Cheng[1*]

Abstract

The proficient handling of diabetic wounds, a rising issue coinciding with the global escalation of diabetes cases, poses significant clinical difficulties. A range of biofunctional dressings have been engineered and produced to expedite the healing process of diabetic wounds. This study proposes a multifunctional hydrogel dressing for diabetic wound healing, which is composed of Polyvinyl Alcohol (PVA) and N^1-(4-boronobenzyl)-N^3-(4-boronophenyl)-N^1, N^1, N^3, N^3-teramethylpropane-1, 3-diaminium (TSPBA), and a dual-drug loaded Gelatin methacryloyl (GM) microgel. The GM microgel is loaded with sodium fusidate (SF) and nanoliposomes (LP) that contain metformin hydrochloride (MH). Notably, adhesive and self-healing properties the hydrogel enhance their therapeutic potential and ease of application. In vitro assessments indicate that SF-infused hydrogel can eliminate more than 98% of bacteria within 24 h and maintain a sustained release over 15 days. Additionally, MH incorporated within the hydrogel has demonstrated effective glucose level regulation for a duration exceeding 15 days. The hydrogel demonstrates a sustained ability to neutralize ROS throughout the entire healing process, predominantly by electron donation and sequestration. This multifunctional hydrogel dressing, which integrated biological functions of efficient bactericidal activity against both *MSSA* and *MRSA* strains, blood glucose modulation, and control of active oxygen levels, has successfully promoted the healing of diabetic wounds in rats in 14 days. The hydrogel dressing exhibited significant effectiveness in facilitating the healing process of diabetic wounds, highlighting its considerable promise for clinical translation.

Keywords Diabetic wound, PVA, Sodium fusidate, Metformin, Microgels, Liposomes

†Rong Chen, Pinkai Wang and Jiajun Xie contributed equally to this work.

*Correspondence:
Zhanjun Shi
shizhanjun111@gmail.com
Jian Wang
wangjiannanfanghospital@gmail.com
Hao Cheng
haocool317@gmail.com
Full list of author information is available at the end of the article

Introduction

The management of diabetic wounds (DW) presents a significant clinical challenge due to their slow healing process, a challenge expected to worsen with the projected increase to over 600 million diabetes cases by 2035 [1]. Diabetic wounds hardly achieve complete healing due to their susceptibility to bacterial invasion, a hyperglycemic environment, and excessive levels of reactive oxygen species (ROS) [2]. Traditional treatments, including oral hypoglycemic agents, antibiotic infusions, and wound disinfection protocols, have often proven inadequate for addressing complex diabetic wounds [3]. Multifunctional wound dressings capable of simultaneously combating infections and mitigating ROS overload have emerged as a promising alternative [4]. However, most current diabetic wound dressing strategies neglect the effective regulation of local glucose levels in the lesions [5]. Elevated glucose levels have been shown to interfere with collagen synthesis and cross-linking through glycosylation, impair angiogenesis, and exacerbate inflammation, thereby perpetuating a detrimental microenvironment and hindering wound healing and tissue regeneration [6]. To achieve rapid and high-quality healing of diabetic wounds, optimal dressings should incorporate the bio functions of antibacterial activity, local glucose regulation, and ROS scavenging [7]. Moreover, dressings with adhesive and self-healing properties are more suitable for clinical application, as they ensure optimal local fixation and durability, thereby reducing the frequency of dressing changes.

Recently, injectable hydrogels and microgels have emerged as promising multifunctional scaffolds. Hydrogel-based dressings are designed to serve as platforms that combine precise and controllable local drug delivery, ROS scavenging, antibacterial effects, and tissue regeneration [8]. ROS-responsive hydrogels demonstrate superior modulation of the local wound microenvironment relative to dressings imbued with active agents like cerium dioxide and curcumin, owing to the inability of these agents to dynamically deplete ROS [9, 10]. Additionally, hydrogel-based dressings excel in moisture retention and wound environment modulation, making them essential for effective wound care [11]. Herein, Polyvinyl Alcohol (PVA) and N^1-(4-boronobenzyl)-N^3-(4-boronophenyl)-N^1, N^1, N^3, N^3-teramethylpropane-1, 3-diaminium (TSPBA) are utilized to form the ROS-responsive hydrogel dressing (PATA hydrogel). This hydrogel is characterized by dynamic phenylboronic ester bonds, exhibiting high reactivity to both extracellular and intracellular ROS [12]. Such reactivity is due to the vacant p-orbital in the boron atoms, which is susceptible to nucleophilic attack by ROS such as hydrogen peroxide (H_2O_2). Consequently, the dynamic phenylboronic ester bonds within the PATA hydrogel can be cleaved in response to excessive ROS and reformed once the ROS is depleted [13]. Given that physiological concentrations of ROS are essential for combating invading pathogens and preventing wound infection, an intelligent PATA hydrogel that can appropriately remove excessive ROS is highly advantageous [14]. The dynamic phenylboronic ester bonds confer shear-thinning and self-healing properties to the PATA hydrogel, which are essential for its injectability and durability [15]. Furthermore, cation-π interactions and π-π stacking occur between benzene rings in PATA hydrogel and metal ions or benzene rings in skin tissues, enhancing the adhesion capabilities of PATA hydrogel dressing [16]. This combination of properties ensures that the PATA hydrogel dressing remains effective and stable in the wound environment, promoting optimal healing conditions.

To impart fast, stable, and long-lasting antimicrobial properties to the dressing, Gelatin Methacrylate (GM) microgels were incorporated into the PATA hydrogel. GM is a photosensitive hydrogel with excellent biocompatibility, widely used in biomedical applications. The nanoscale porous structures in GM microgels anchor nanostructures (e.g., liposomes) while allowing the diffusion of small molecules [17]. Their unique properties and drug release characteristics allow for customization through different microgel combinations tailored for specific biological responses, offering versatile therapeutic uses. Microgels can be produced using several methods, including intermittent emulsion, microfluidics, and photolithography [18–20]. The microfluidic method offers significant advantages: adjusting the channel diameter and flow rate yields monodisperse microgels with precise control over release and degradation, while gentle manufacturing conditions maintain drug activity, enabling the in situ encapsulation of bioactive molecules [21]. For efficient and specific bacterial eradication, Sodium fusidate (SF) is loaded in the GM microgels. SF is particularly effective against Gram-positive bacteria like *Staphylococcus aureus*, the primary pathogen in infectious diabetic wounds [22]. Specifically, SF inhibits ribosome translocation in bacteria by targeting and interfering with bacterial elongation factor G (EF-G), thereby blocking bacterial protein synthesis and eradicating bacteria without toxicity to human cells [23]. The local application of SF allows for more effective concentration at diabetic lesions, despite the compromised microcirculation in diabetic patients, and reduces the likelihood of bacterial resistance development [24].

To address the high local glucose levels in diabetic lesions over the long term, Metformin Hydrochloride (MH) is used. MH is a stable and efficient drug widely used for diabetes, enhancing insulin responsiveness and reducing hepatic gluconeogenesis. For sustainable delivery, MH is loaded into a secondary vehicle [25, 26]. Nanoliposomes (LP) are recognized as a classic lipid spherical vesicle for drug delivery, contributing an extra protective layer for loaded drugs, prolonging their half-life, and ensuring an optimal therapeutic concentration range [27]. However, pure LP suffers the risk of premature drug leakage and release before reaching the targeted site [28, 29]. Encapsulating LP into GM microgels is proven to significantly prevent premature aggregation and fusion and enhance the stability of LP, for the non-covalent interactions between nitrogen and oxygen in GM microgels and phospholipids in LP anchor the lipid vesicle in the microgel network [29].

In this study, we developed an injectable, self-healing, and adhesive hydrogel/microgel-based dressing, aiming at addressing infectious diabetic wounds and achieving fast and high-quality healing. SF and MH-loaded LP (LP (MH)) were encapsulated into GM microgels to realize the controlled release pattern, contributing as a multi-functional element to eradicating bacteria and simultaneously alleviating glucose levels in diabetic lesions. The PATA hydrogel serves as an intelligent ROS-consuming matrix with injectable, durable, and adhesive properties, integrating GM microgels to ensure precise and concentrated drug delivery in the wound region. We conducted the construction and comprehensive characterization of the PATA-GM (SF/LP) dressing, evaluating its antimicrobial activity, ROS elimination, and hyperglycemia reduction through in vitro experiments. In vivo experiments involved a rat model of type I diabetes, assessing the pro-healing ability of infected diabetic wounds using pathology and imaging analyses. It is hypothesized that the dressings developed in this study enhance the modulation of the local microenvironment in infected diabetic wounds, thereby promoting wound healing. Taken together, our multi-functional hydrogel/microgel-based dressing possesses promising potential and offers a novel strategy for infectious diabetic wound management.

Materials and methods

Materials

4-(Bromomethyl) phenylboronic acid (C_7H_8BBrO, 98%), Poly (vinyl alcohol) 1788 (PVA, 87–90% hydrolyze), 4-(Bromomethyl) phenylboronic acid ($C_7H_8BBrO_2$, 98), Sodium fusidate (SF, $C_{31}H_{47}NaO_6$, 98%), metformin hydrochloride (MH, $C_4H_{11}N_5{\cdot}HCl$, 97%), Gelatin methacryloyl (GM-30%), phalloidin-TRITC ($C_{60}H_{70}N_{12}O_{13}S_2$), Span 80 ($C_{24}H_{44}O$), paraffin oil (AR 98%), Distearoylphosphatidylethanolamine-polyethylene glycol (DSPE-PEG2000, 99%), Lecithin ($C_{42}H_{80}NO_8P$, 90%), N, N, N′, N′-Tetramethyl-1,3-propanediamine (99%), Cholesterol ($C_{27}H_{46}O$, 95%), 15-mL centrifuge tubes, iFluor 488 phalloidin, RNAisoPlus kit (Takara Corp, Shiga, Japan), 200-μL and 1-mL pipette tips, 4′,6-diamidino-2-phenylindole (DAPI), 24-well and 96-well plates, CCK-8 cell viability reagent, and phosphate-buffered saline (PBS) were acquired from Macklin (Shanghai, China). Citric acid monohydrate, dihydrate, sodium citrate, and streptozotocin were purchased from Aladdin Company (Shanghai, China). Micropump injector (LEADFLUID TYD01, Baoding, China), SYBR Green Real-Time PCR Master Mixes (Thermo Fisher Scientific), SYP-TS hydraulic press (Lith Machine Limited, Xiamen, China), model NLFY-60 (Tianjin, China), Instron 5943 universal material tester (MA, USA), FT-IR instrument (Thermo Scientific Nicolet iS10 infrared FT-IR spectrometer, MA, USA). Rat L929 cell lines were procured from Cyagen (Jiangsu, China). ATCC 25923 (*MSSA*), ATCC 43300 (*MRSA*), and ATCC 25922 (*E.coli*) were obtained from ATCC (Manassas, VA, USA).

Synthesis of PATA-based codelivery hydrogel

Synthesis of nanoliposome

Nanoliposome (LP) was fabricated using the thin film dispersion technique [30]. The procedure involved dissolving 20 mg of soy lecithin, 6 mg of cholesterol, and 6 mg of Distearoylphosphatidylethanolamine-polyethylene glycol (DSPE-PEG 2000) each in 1 mL of chloroform in a 1.5 mL EP tube. The mixture was then transferred to a 100 mL round-bottom flask and supplemented with an additional 2 mL of chloroform. Using a rotary evaporator (LICHEN, Henan, China) under vacuum (110 rpm, 45 °C), the chloroform was evaporated, forming a lipid film inside the flask. Subsequently, 5 mL of an aqueous solution of fully dissolved metformin hydrochloride (MH) was added, and the flask was rotated for 5 min. The final step involved sonication with a high-intensity probe sonicator (JY92-IIN, Scientz, China) at 25 °C (60 plus/min, 130 W) for 5 min, resulting in single-layer nanoliposomes with decreased particle sizes.

Synthesis of GM (SF/LP) microgels

Gelatin methacryloyl (GM) synthesis adhered to established protocols [31]. The subsequent procedure involved crafting GM microgel through a microfluidic emulsion method, utilizing a coaxial needle and dual syringe pumps (LEADFLUID TYD 01, Baoding, China). In this process, sodium fusidate (SF) was

homogeneously incorporated into a 10 w/v% GM polymer solution containing MH-enriched LP. The oil phase, consisting of paraffin oil, was combined with the surfactant Span 80 (5 w/v%). Upon integration of the oil phase with the aqueous phase, the water-to-oil flow rate ratio was rigorously controlled between 0.08 and 0.1 (100 μL/min for the oil, 8–10 μL/min for the aqueous phase) [17]. The aqueous phase, containing 5 wt% GM, 2.5 wt% MH-loaded LP, and 0.5 wt% photoinitiator dissolved in PBS, alongside the oil phase, comprising 5 wt% Span80 in paraffin oil, were concurrently administered into inlets of the microfluidic device using syringes. The formation of emulsion droplets ensued, which were then subjected to ultraviolet (UV) radiation (64 mW/cm^2, 360–480 nm) for a minute to initiate photo-crosslinking. The final step entailed centrifugation (6000 rpm, 4 min) to collect the formed crosslinked microgels containing SF and MH-loaded LP.

Synthesis of ROS-responsive TSPBA linker

TSPBA was synthesized through an acetal reaction between N, N, N′, N'-Tetramethyl-1,3-propanediamine (TMPDA), and 4-(bromomethyl) phenylboronic acid (4-BPBA), following established methods [32]. Initially, 1.31 g of 4-BPBA was dissolved in 100 mL of dimethylformamide (DMF). After complete dissolution and sonication for 10 min, 260 mg of TMPDA was added to the mixture and placed on a magnetic stirrer (60 °C, 24 h). Adding tetrahydrofuran (THF) and centrifuging the solution (10,000 rpm, 5 min) resulted in a precipitate, which was lyophilized to obtain the final TSPBA product.

Preparation of PATA-GM (SF/LP) hydrogel

PATA hydrogels were made by mixing PVA and TSPBA. Based on previous studies [32], PVA was utilized in varying concentrations (3, 6, and 9 w/v%), combined with TSPBA (3 w/v%), to explore the gelation efficiency at different PATA ratios. Upon establishing the optimal PVA concentration, the PVA was then integrated with GM containing SF (0.1 w/v%), and MH-loaded LP (1 w/v%). Then 3 w/v% of TSPBA was added to form a ductile gel matrix [33]. After lyophilization, the structural integrity of the PATA-based hydrogels was scrutinized using an electron scanning microscope (SEM).

Fourier transform infrared (FT-IR) analysis of the PATA-based hydrogels

The FT-IR spectroscopy (Horiba, Kyoto, Japan) analysis was conducted to examine the functional groups within the GM, boronic acid bonds, and the PATA-based co-delivery hydrogel. The spectral range between 4000 and 600 cm^{-1} was meticulously analyzed against a backdrop of potassium bromide (KBr) and ambient air.

SEM scan of the PATA-based hydrogels

Morphological and porosity attributes of the hydrogels were assessed using an SEM (ZEISS Sigma 300 SEM, Jena, Germany). For SEM analysis, a central section of the freeze-dried hydrogel was prepared. ImageJ software (v1.53) was employed to quantify the average porosity of the hydrogel.

Rheological test of PATA-based hydrogels

Dynamic monitoring of borate-mediated cross-linking kinetics within hydrogels was conducted using a Discovery HR-2 Rheometer (TA Instruments, DE, UK) outfitted with an 8 mm diameter steel parallel plate. The methodology involved the immediate mixing and deposition of the PVA-containing GM (SF/LP) and TSPBA solutions onto the plate, followed by rheological evaluation at a consistent temperature of 25 °C. Rheological properties were assessed under a constant strain of 1% across a frequency spectrum of 0.1 to 100 rad/s at 25 °C. The quantitative assessment of the self-healing capabilities of the samples was performed by tracking the changes in the storage (G′) and loss (G″) moduli of the PATA-GM (SF/LP) hydrogels throughout cycles of destructive shearing (an oscillatory strain sweep elevating the strain from 0.1% to 1000% at a constant frequency of 1 Hz) and subsequent recovery (an oscillatory time sweep at a strain of 0.5% and a frequency of 1 Hz for 60 s).

Swelling and degradation rate of PATA-based hydrogels

In the experiment, samples were divided into four categories: PATA, PATA-GM (SF), PATA-GM (LP), and PATA-GM (SF/LP). These groups were equilibrated for 2 h in PBS at 37 °C, post which they were weighed on a microbalance (PUCHUN JA GW 0.001 g SERIES, Shanghai, China), and their masses were documented as M (s). Following this, they were pre-cooled in a lyophilizer at − 80 °C for 8 h and then vacuum-dried for 12 h. The mass of the samples after freeze-drying was recorded as M (l). The swelling rate of the hydrogel sample was computed using the formula:

$$Swelling\ ratio = (M(s) - M(l))/M(l) \times 100\%. \quad (1)$$

Post-equilibration, the hydrogel specimens underwent incubation in PBS with varying H_2O_2 concentrations (0 mM, 0.01 mM, 0.1 mM, and 1 mM) at 37 °C. To evaluate their degradation kinetic, we measured the residual mass of these freeze-dried specimens at designated

intervals, identified as M (b). Subsequently, these measurements were compared with the initial dry weight using a designated formula for analytical purposes.

$$Degradation\ ratio = M(b)/M(l) \times 100\%. \quad (2)$$

Characterization of SF and MH release dynamics

To ascertain the total release of SF and MH from PATA-based hydrogels, baseline calibration was conducted using UV–visible spectroscopy (NanoDrop™ 2000/2000c spectrophotometer, Thermo Fisher Scientific, Waltham, Massachusetts, USA). Calibration involved measuring the absorbance of varying concentrations of SF and MH solutions (ranging from 1 to 200 mg/mL in deionized water). Distinct absorption peaks for SF and MH were identified at wavelengths of 290 nm and 233 nm, respectively. Following this, explorations into the release dynamics of SF and MH from the hydrogels commenced. The formulation, comprising both SF and MH-loaded LP, was amalgamated with a solution containing PVA (9 w/v%) prepolymer and TSPBA (3 w/v%). The fabricated hydrogels were allocated into 12-well plates containing PBS, with selected wells also incorporating 100 μM H_2O_2, and were incubated at 37 °C. Periodically, 1 mL of the solution was extracted from each well and substituted with an equivalent volume of fresh solution. Absorbance readings at 290 nm and 233 nm were subsequently recorded and utilized to determine the release quantities of SF and MH by comparison with a standard curve.

In vitro cellular cultivation

L929 cells maintained up to the 5th passage, were employed to determine the biocompatibility of the PATA-based hydrogel [34]. These cells were propagated in DMEM enriched with 10% fetal bovine serum, in an environment of 5% CO_2 at 37 °C, with the medium being refreshed bi-daily. For biocompatibility assessment, L929 cells were incubated alongside the hydrogel specimens, followed by their analysis using live/dead cell staining assay and the CCK-8 assay.

Cell viability assay

Cell viability of L929 cells, in co-culture with hydrogel samples, was evaluated using the CCK-8 assay. L929 cells (1×10^5 cells/mL) were co-cultured with PATA-based hydrogel at 37 °C in a 5% CO_2 environment for intervals of 6 and 12 h. The absorbance of the supernatant was measured at 450 nm using a microplate reader (Tecan Trading AG, Switzerland). Cell viability in the CCK-8 assay was computed using the formula:

$$Cell\ viability(\%) = (measured\ value - blank\ value) / (control\ value - blank\ value) \times 100\% \quad (3)$$

In this formula, the "blank value" refers to DMEM enhanced with 10% fetal bovine serum. The "control value" is associated with the spectral data obtained from the cell culture medium, whereas the "measured value" corresponds to the readings from the medium co-cultured with PATA-based hydrogels.

To evaluate cell viability when L929 cells were co-cultured with various substrates, a fluorescence-based live/dead viability kit (Calcein-AM/PI Double Stain Kit, YEASEN, Shanghai, China) was utilized, adhering to the guidelines of the manufacturer. Following pre-determined time points, cells in co-culture with hydrogels were stained and then incubated for 20 min in darkness. Subsequently, these cells underwent triple washing with PBS. Fluorescence microscopy (ECLIPSE Ti2-E, Nikon, Japan) was used to capture images of the stained samples. Viability analysis, distinguishing live cells (green fluorescence) from dead cells (red fluorescence), was conducted using ImageJ software (v1.53). The viability of the cell was quantified using a specific formula:

$$Cell\ viability(\%) = number\ of\ live\ cells / \left(number\ of\ live\ cells + number\ of\ dead\ cells\right) \times 100\% \quad (4)$$

Cell proliferation assay

During the cell proliferation evaluation, cells were stained according to the specified protocols of the manufacturer, using iFluor 488 phalloidin and 4',6-diamidino-2-phenylindole (DAPI). IFluor 488 phalloidin required a 4-h incubation at 37 °C and DAPI staining required a 30-min incubation. After incubation, the samples were washed three times with PBS. These stained cells were then observed using an inverted fluorescence microscope (ECLIPSE Ti2-E, Nikon, Japan). Image analysis was carried out using ImageJ software (v1.53), which was instrumental in examining the acquired images.

Antibacterial assay

The bacterial strains ATCC 25923 (*MSSA*), ATCC 43300 (*MRSA*), and *E.coli* (ATCC 25922) were grown in 4 mL of Luria–Bertani (LB) broth for 18 h. Subsequently, a solution with 1 mL of LB and a bacterial concentration of 1.0×10^6 CFU/mL was prepared and added to a 24-well plate. This arrangement was then co-incubated with various compounds such as PATA, PATA-GM (SF), PATA-GM (LP), or PATA-GM (SF/LP) at a constant temperature of 37 °C for time intervals of 6, 12, and 24 h.

After incubation, the bacteria were harvested and underwent a washing process using PBS buffer with pH values of 6.3 or 7.4, at a centrifugation speed of 3000 rpm. The bacterial cultures were then stained using a live/dead bacterial staining agent for 15 min and visualized under an inverted fluorescence microscope (ECLIPSE Ti2-E, Nikon, Japan).

The antibacterial efficacy of the hydrogel samples was evaluated using an inhibition zone assay against two bacterial strains. After a 24-h incubation at 37 °C, the zones indicative of bacterial growth suppression were captured and quantified digitally, employing ImageJ software (v1.53) for analysis.

Antibiofilm assay

The efficacy of biofilm eradication was confirmed via scanning electron microscopy (SEM) analysis. For biofilm formation, 1 mL aliquots of *MSSA*, *MRSA*, and *E. coli* suspensions (1×10^8 CFU/mL) were inoculated into individual wells of a 24-well plate containing titanium sheets, followed by a two-day incubation with daily LB medium replacement and co-culture with PATA-based hydrogels. The titanium sheets with biofilms were fixed in 2.5% GA at 4 °C for 12 h, dehydrated through an ethanol gradient (50%, 60%, 70%, 80%, 90%, and 100%) for 10 min each at 25 °C [35], freeze-dried, and gold-sputtered. SEM (Sigma 300, ZEISS, Germany) was then employed for visualization.

Evaluation of mimetic activity in superoxide dismutase (SOD) analogs

The superoxide anion scavenging ability of the boronate ester was assessed using the SOD assay kit-WST (Sigma-Aldrich, St. Louis, USA) was utilized. The process involved immersing the PATA-based hydrogel in the assay solution, followed by measuring the optical density of the resultant supernatant at 450 nm. The SOD activity was calculated using the method prescribed by the manufacturer of the kit. Below is the formula used for calculating the SOD assay outcomes:

$$\begin{aligned} SOD\ activity\left(U/10^4 cell\right) &= [inhibition\ percentage \div \left(1 - inhibition\ percentage\right) \times Vanti - total] \\ &\div (500 \times V\ sample \div V\ sample \div V\ sample\ total) \times F \\ &= 0.02 \times inhibtion\ percentage \div (1 - inhibition\ percentage) \times F \end{aligned} \tag{5}$$

In this formula, "V total" denotes the overall reaction volume, which is 0.2 mL. "V sample" represents the volume of the sample introduced into the reaction system, set at 0.02 mL. "V sample total" refers to the total volume of the extract added, being 1 mL. The concentration of the protein sample, "Cpr", is expressed in mg/mL. "W" indicates the mass of the sample in grams. The numeral 500 corresponds to the total cell or bacterial count, equivalent to 5 million. Lastly, "F" signifies the dilution factor applied to the sample.

Assessment of catalase (CAT)-like activity in PATA-based hydrogels

To investigate the CAT-mimetic activity of PATA-based hydrogels, the Amplex Red reagent assay kit (Sigma-Aldrich, St. Louis, USA) was used, drawing on established research methods. The process began with the incubation of PATA-based hydrogel samples in 5 μM hydrogen peroxide. This was followed by the addition of Amplex Red and horseradish peroxidase, triggering a reaction with remaining H_2O_2. Fluorescence emitted by resorufin was quantified at a wavelength of 571 nm:

$$\begin{aligned} CAT\left(U/10^4 cell\right) &= \left[\Delta A \times Vrt \div (\varepsilon \times d) \times 10^6\right] \\ &\div (V_s \div V_{st} \times 500) \div T = 1.529 \times \Delta A \end{aligned} \tag{6}$$

In this formula, "V_{rt}" represents the total volume, which is 2×10^{-4} L. The molar extinction coefficient of H_2O_2, denoted by "ε", is 43.6 L/mol/cm. The optical path length for a 96-well plate, labeled as "d", measures 0.6 cm. "V_s" stands for the volume of the sample added, amounting to 0.01 mL. "V_{st}" refers to the volume of the extract added, which is 1 mL. The duration of the reaction, "T", is set at 1 min. The figure 500 indicates the total cell or bacterial count, equating to 5 million. Lastly, the unit conversion factor, represented by "10^6", defines the relationship where 1 mol equals 10^6 μmol.

Cellular ROS scavenging activity

To evaluate the intracellular ROS-scavenging efficiency of PATA, PATA-GM (SF), PATA-GM (LP), and PATA-GM (SF/LP) hydrogels, L929 cells were incubated with these hydrogels in a 12-well format. The culture medium contained 100 μM H_2O_2 and was sustained for 2 h. Following this, DCFH-DA staining was utilized to mark intracellular ROS, and the fluorescence intensity indicative of ROS levels was quantitatively assessed using ImageJ software (v1.53).

In vitro hyperglycemia reducing assay

The glucose uptake by L929 cells was determined using a modified protocol from a glucose assay kit (Glucose Assay Kit with O-toluidine, Beyotime, Shanghai, China). Glucose calibration curves were established using the glucose standards from the kit, ranging from 5 to 2000 mg/dL. After establishing the glucose standard curve, we analyzed the variations in glucose concentration in the supernatant of the medium that had been co-cultured with hydrogels. L929 cells were cultured in 24-well plates at a density of 4×10^4 cells/well and incubated for 24 h to allow attachment. Cells in 5.5 mM glucose serum-free DMEM were incubated for 12 h. Post incubation, L929 cells were treated with 10% serum DMEM supplemented with PATA, PATA-GM (SF), PATA-GM (LP), and PATA-GM (SF/LP) for 24 h. To quantify variations in glucose levels within the culture medium, a 5 μL volume of the cell culture supernatant was dispensed into a 1.5 mL ep tube containing 185 μL of Glucose Assay Reagent. This assembly was then incubated in a water bath at 95 °C for 8 min, followed by rapid cooling in an ice bath at 4 °C for 5 min. Subsequently, the reaction mixture from the ep tube was transferred to a 96-well plate for absorbance measurement at 630 nm using a microplate reader (Tecan Trading AG, Switzerland), with the outcomes being meticulously documented. This procedure was replicated thrice.

Preparation of diabetic SD rats

Animal experiments were approved by the Institutional Animal Care and Use Committee at Nanfang Hospital, Southern Medical University (R202009.05, Guangzhou, China). All procedures conformed to the National Institute of Health's Guide for the Care and Use of Laboratory Animals (NIH Publications No. 8023, revised 1978). The study involved 25 male Sprague–Dawley (SD) rats, each weighing approximately 200 g, distributed into five groups: Control, PATA, PATA-GM (SF), PATA-GM (LP), and PATA-GM (SF/LP), sourced from the Experimental Animal Center at Southern Medical University. A type-1 diabetes model was established in these rats, following established methodologies, by administering intraperitoneal injections of streptozotocin (from Aladdin Company, Shanghai, China) at doses of 50–60 mg/kg body weight. Glucose levels in rat blood were monitored on days 0, 1, 3, 7, and 14, with samples collected from the tail vein and analyzed using a Bayer Contour Next EZ meter (Leverkusen, Germany). Rats with blood glucose levels exceeding 11.1 mmol/L were identified as diabetic.

Animal procedures and surgeries

In this study, 25 male SD rats, each weighing around 200 g, were utilized. They were divided into five groups: Control, PATA, PATA-GM (SF), PATA-GM (LP), and PATA-GM (SF/LP), sourced from the Experimental Animal Center at Southern Medical University. Anesthesia was induced using a 3% pentobarbital sodium solution, administered intraperitoneally at 100 μL per 100 g of body weight. Following fur removal and sterilisation, a full-thickness skin wound of 1.0 cm diameter was created on the dorsal surface of each rat. Each wound was then inoculated with 20.0 μL of ATCC 25923 (*MSSA*) suspension (1×10^8 CFU/mL). A gauze was placed over the wounds for 6–8 h to initiate infection. Afterwards, the designated hydrogel dressings—PATA, PATA-GM (SF), PATA-GM (LP), and PATA-GM (SF/LP)—were applied to the wounds. Wound healing was monitored and photographed on days 0, 1, 3, 7, and 14 post-treatment.

Statistical analysis

Data from all experiments underwent statistical analysis using one-way ANOVA and Bonferroni's post hoc test, employing GraphPad Prism 8.0 software for the computation. The error bars in the graphical representations indicate the mean ± standard deviation (SD) of the data collected ($^*P<0.05$).

Results

Hydrogel fabrication and characterization

The fabrication process for PATA-based hydrogels is illustrated in Fig. 1 and Fig. S1. The ROS-responsive TSPBA linker was synthesized and then characterized by Nuclear magnetic resonance spectroscopy (^{1}H-NMR) (Fig. S2) [36, 37]. We investigated the impact of varying PVA and TSPBA concentrations on gel flexibility (Fig. S3a). A concentration of 3% TSPBA effectively cross-linked with 9% PVA, resulting in a flexible gel. Lowering the PVA concentration further prevented gel formation. Consequently, we identified the optimal concentrations as 9% PVA and 3% TSPBA (w/v) (Fig. S3a). As shown in Fig. S4, a hydrogel can be formed by cross-linking within 10 s using the TSPBA and hydrogel/microgel system (PVA-GM (SF/LP)), consistent with the rheological test results in Fig. 2c. GM microgel visualized under microscopy had an average diameter of approximately 300 μm (Fig. S3b(iii)). Dail staining was employed to visualize LP encapsulated within GM microgel (Fig. 3a(iv); Fig. S3b(i)-(ii)). The majority of LP particles measured 100–150 nm in size (Fig. 2d), with an encapsulation efficiency for MH at 35.68 ± 6.144% (Fig. S5b). The LP had a zeta potential of -2 (Fig. S5c), indicating a likelihood

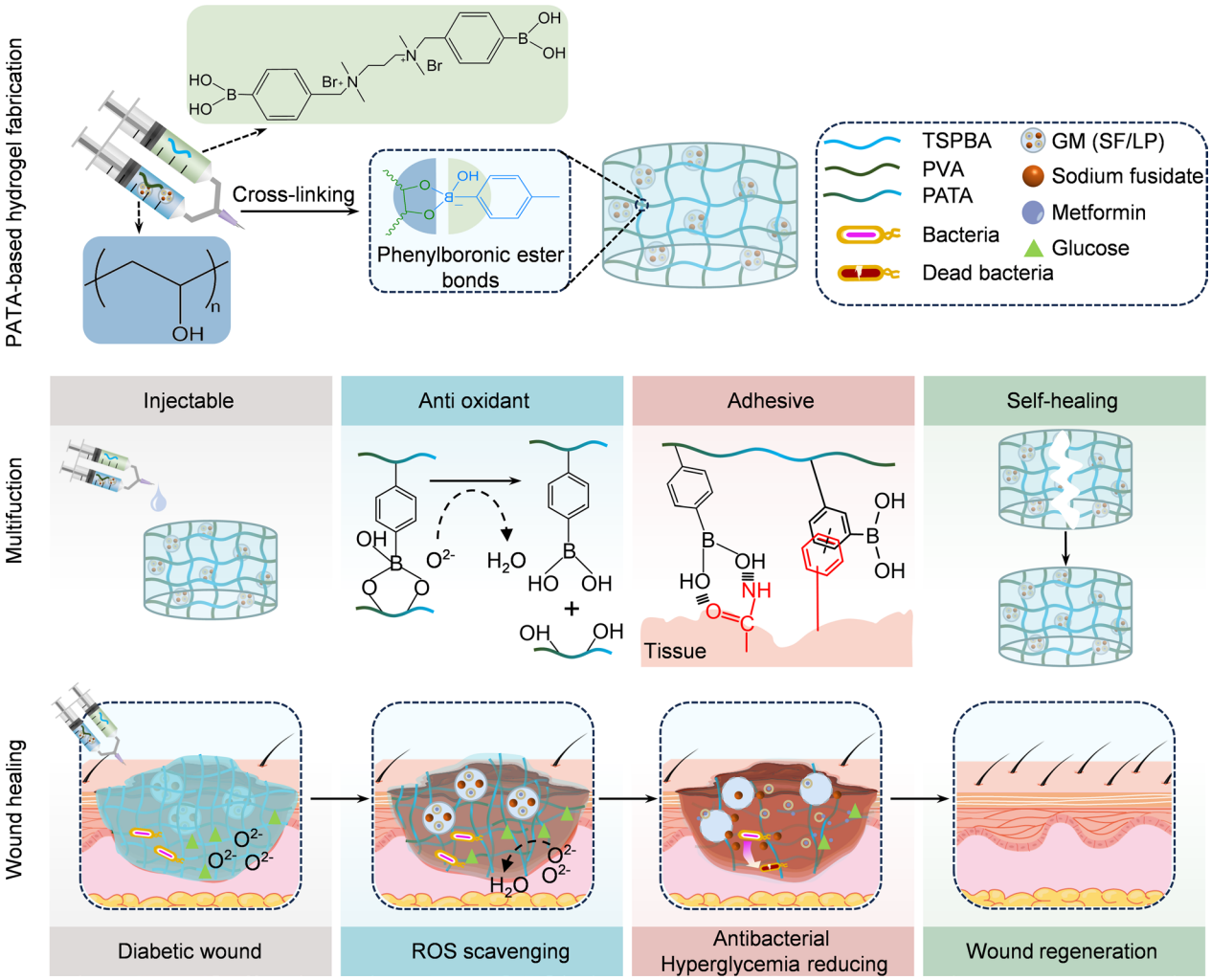

Fig. 1 Schematic depicting the role of PATA-based hydrogel dressings in facilitating the healing process of infected diabetic wounds

of particle aggregation. GM gel microspheres were used to improve LP stability. Under SEM, LP homogeneously dispersed on the surface of GM microgel (Fig. 2ai). PATA hydrogel demonstrated a porous interconnected microstructure with encapsulated GM microgel (Fig. 2aii–iii). The porosity of PATA-based hydrogel was 22.11 ± 5.244% (Fig. S5d). The FT-IR spectra indicate comparable absorption peaks for the PATA-based hydrogels. The unique peaks at 1720 cm^{-1} and 1250 cm^{-1} correspond to the C=O double bond and the C–O–C stretching vibration of the methacrylic acid group. The resonance found at 1375 cm^{-1} is linked to B–O stretching vibration, derived from the boronate ester linkage, consistent with previous studies [38]. Oscillatory rheological analysis was employed to evaluate the mechanical characteristics of the PATA-GM (SF/LP) hydrogel. Over time of 0 to 300 s, the storage modulus (G′) of the hydrogel exhibited variations ranging from 24.39621 to 159.4434 Pa. In contrast, the loss modulus (G″) demonstrated a range from 14.18528 to 51.23182 Pa (Fig. 2c). In our study, PATA-GM (Liposome) without SF and MH loading was used as a control group. The absorbance values at 290 nm and 233 nm of the control group were subtracted in the cumulative release experiments (Fig. S9), and the cumulative drug release was then calculated (Fig. 2e, f). Figure 2e, f show that in a PBS medium with 100 μM H_2O_2, the hydrogels containing SF-loaded GM and MH-loaded LP released about 76.14 ± 2.33% and 73.946 ± 1.049% of the drug over 15 days. In contrast, in PBS without H_2O_2, the drug release from the hydrogels was much lower, 40.809 ± 3.055% (SF-loaded GM) and 45.762 ± 8.205% (MH-loaded LP) in the same timeframe. Figure 2g indicates that the degradation rate of PATA hydrogels increased with higher H_2O_2 concentrations. In 0 mM and 0.01 mM H_2O_2 environment, the hydrogels underwent incomplete degradation, with

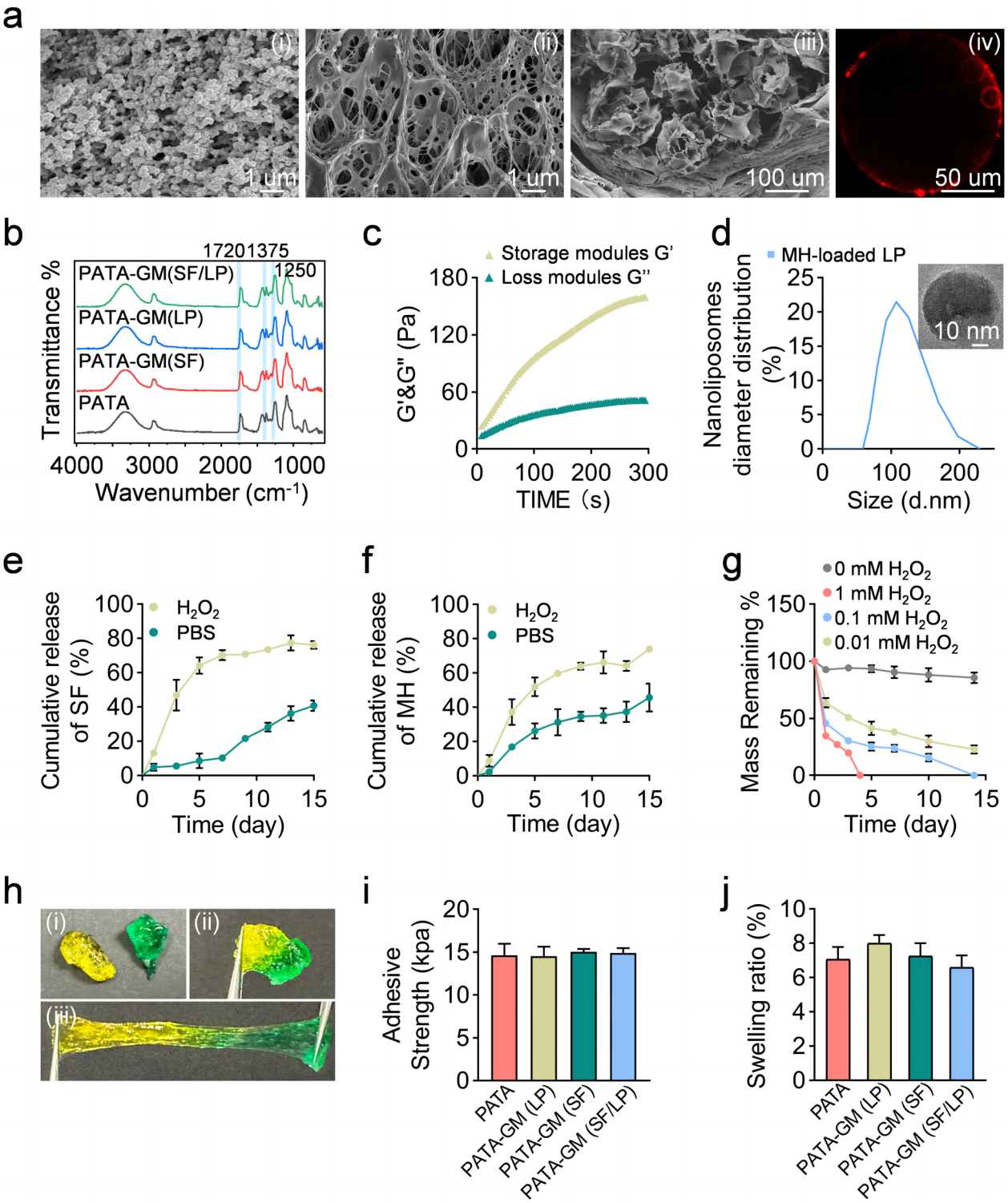

Fig. 2 Synthesis and Analysis of PATA-based Hydrogel: **a**, i Surface morphology of LP-incorporated GM microgels captured via SEM; (**a**, ii–iii) SEM of PATA hydrogels and GM microgels-loaded PATA hydrogel; (**a**, iv) Visualization of Dail-Stained LP on GM Microgel Surfaces via TRITC Fluorescence Imaging; **b** FT-IR analysis of PATA-based hydrogels; **c** Rheological analysis of PATA-GM (SF/LP) hydrogel; **d** Measurement of LP particle size; **e, f** Cumulative release profile of SF and MH encapsulated in PATA-GM (SF/LP) hydrogel; **g** Degradation rate of PATA hydrogel in different concentrations of H_2O_2; **h** Image of self-healing capabilities of PATA hydrogel; **i, j** Adhesive strength and swelling ratio of PATA-based hydrogel; *$P < 0.05$

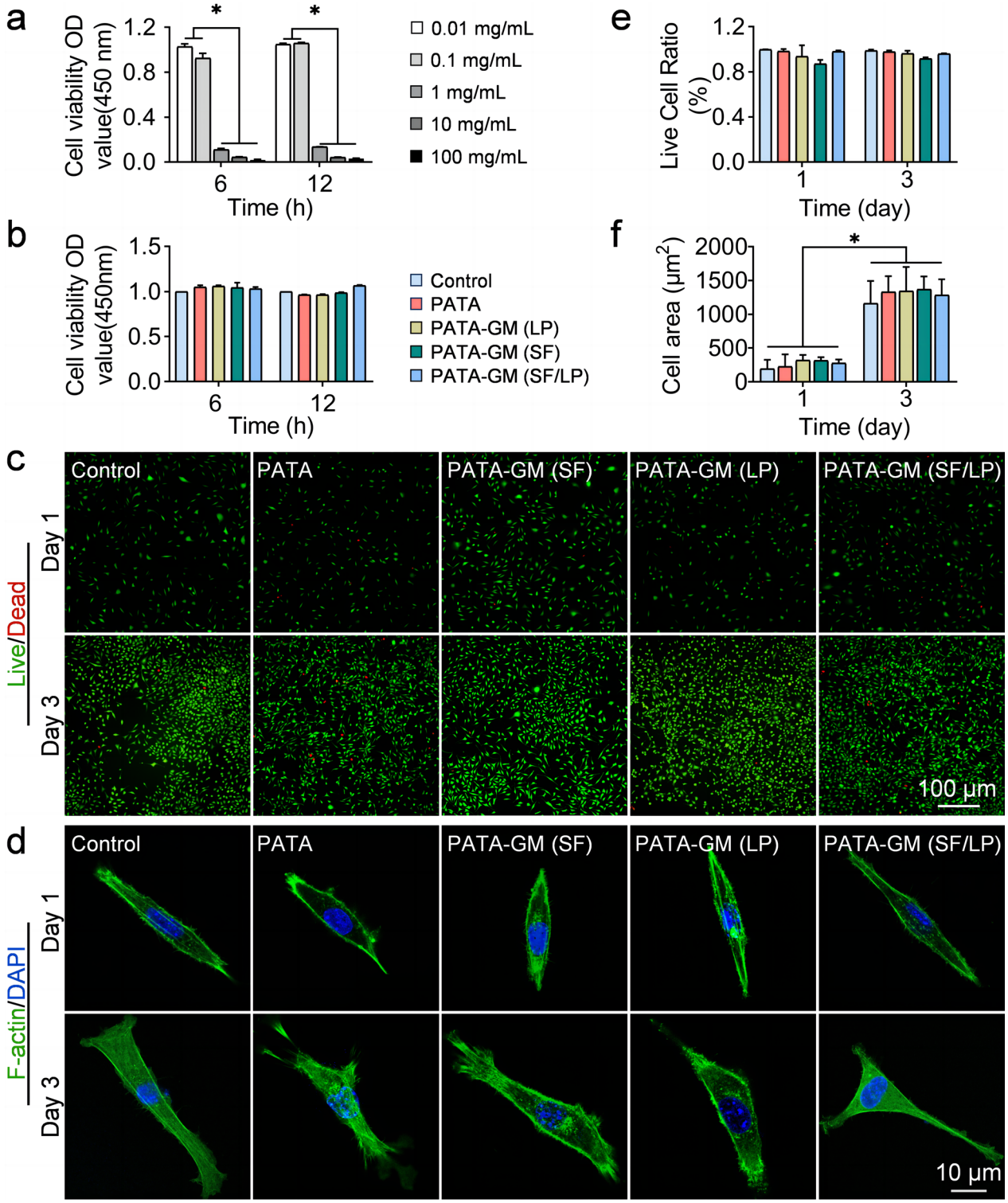

Fig. 3 Assessment of cytotoxicity in PATA-based co-delivery hydrogels: **a** CCK-8 assay results for L929 cells exposed to varying concentrations of SF; **b** CCK-8 assay for L929 cells incubated with PATA-based hydrogels; **c** Evaluation of cell viability in L929 cells co-cultured with different PATA-based hydrogels, using live/dead staining on days 1 and 3 (live cells indicated by green fluorescence, dead cells by red fluorescence); **d** Proliferation of L929 cells on PATA-based hydrogels, visualized through phalloidin and DAPI staining at days 1 and 3; **e** Analysis of cell viability; **f** Quantification of L929 cell area to assess cell proliferation on PATA-based hydrogels; *$P < 0.05$

85.567 ± 4.626% and 22.790 ± 3.504% of the material remaining undegraded, respectively. In contrast, complete degradation occurred within 5 days in 1 mM H_2O_2, while 0.1 mM H_2O_2 took 14 days for complete disintegration. The self-healing capability of the PATA hydrogel, attributed to its dynamic boronic ester covalent bonds, was further investigated. Figure 2h demonstrates that upon bringing two separate segments of the hydrogel into proximity, they naturally self-healed in under one minute. Fig. S8 displays the changes in storage modulus (G') and loss modulus (G") of the PATA hydrogels when subjected to varying frequencies. PATA-based hydrogels demonstrated a similar swelling ratio (7.057 ± 0.725%, 7.998 ± 0.492%, 7.245 ± 0.769%, 6.592 ± 0.709%) (Fig. 2j) and adhesive strength (14.612 ± 1.376 kpa, 14.520 ± 1.129 kpa, 15.047 ± 0.326 kpa, 14.893 ± 0.564 kpa) (Fig. 2i). The addition of SF and LP (MH) loaded microgel did not affect the above two characteristics. The PATA hydrogel also exhibits strong adhesive properties on various surfaces (Fig. S6).

Cell prliferation and viability assays

Figure 3a and Fig. S10 depict that CCK-8 assay outcomes reveal a decline in L929 cell viability at SF concentrations exceeding 100 μg/mL and MH concentrations surpassing 10 mg/mL. Optimal drug concentrations ensured that simultaneous encapsulation of both SF and MH did not enhance hydrogel cytotoxicity, as illustrated in Fig. 3b. Figure 3c–f showcase live and dead cell staining results, along with comparable cell viability (> 90%) and cell count in cultures involving PATA-based hydrogel.

In vitro antimicrobial activity, inhibition zone assay, and antibiofilm properties of the hydrogel

Figure 4a, b illustrates the bacterial staining results when exposed to PATA-based hydrogels. A significant reduction in bacterial presence was observed within 12 h (Fig. S12a, b), culminating in the over 98% elimination of bacteria by the 24-h interval (Fig. 4a, b). Hydrogels infused with SF demonstrated enhanced antibacterial properties in comparison to their SF-absent counterparts, as depicted in Fig. 4d-e; Fig. S12c-d, S13a-b. These outcomes, derived from live/dead bacterial staining, are consistent with the data obtained from the zone of inhibition assays. SF demonstrates a more specific bactericidal effect against S. aureus and a relatively lower efficacy against E. coli. In the conducted zone inhibition assays, these hydrogels exhibited diameters of inhibition zones measuring 2.932 ± 0.263 cm and 3.09 ± 0.126 cm against ATCC 25923 (*MSSA*), and 2.98 ± 0.194 cm and 3.34 ± 0.244 cm against ATCC 43300 (*MRSA*), for PATA-GM (SF) and PATA-GM (SF/LP), correspondingly, as detailed in Fig. 4c and f.

SEM analysis revealed that SF-loaded hydrogels effectively inhibited bacterial proliferation, as detailed in Fig. S14. Following SF incorporation, there was a noticeable dispersion of *MSSA* and *MRSA* biofilms, along with a significant increase in the number of lysed bacteria. In contrast, the *E. coli* biofilm exhibited partial dispersion. Without SF, PATA-GM (LP) displayed biofilm disruption similar to the PATA group. Notably, biofilm disruption in the PATA and PATA-GM (LP) groups may be attributed to the quaternary amine motifs in TSPBA.

Quantitative real-time PCR (qRT-PCR) analysis of antibacterial relative gene expressions

For qRT-PCR validation, the biomarkers selected included feoB, fusD, ftnA, fusA, sufU, dnaK, and groL. As depicted in Fig. 4g–j and Fig. S12e–g, the relative gene expression value for fusA, a gene implicated in the regulation of staphylococcal EF-G proteins, was observed 109.840 ± 6.384-fold in ATCC 25923 (*MSSA*) and 34.9 ± 5.280-fold in ATCC 43300 (*MRSA*) higher compared control group, consisted with previous studies [39]. Genes associated with bacterial metabolism, namely feoB, fusD, ftnA, dnaK, and groL, exhibited a more marked upregulation in ATCC 25923 (*MSSA*), whereas their expression increase in ATCC 43300 (*MRSA*) was not significant.

In vitro antioxidant and hyperglycemia reducing activity of PATA-based hydrogel

The evaluation of the antioxidant capacity of PATA-based hydrogels involved analyzing SOD mimetic activities, CAT mimetic activities, and intracellular ROS, as delineated in Fig. 5. Results from the SOD and CAT assays indicated a reduction in SOD activity and formaldehyde concentration in the supernatant of cells incubated with PATA-based hydrogels compared to the control group ($P < 0.05$), signifying diminished oxidative stress on the cells. Additionally, the effectiveness of PATA-based hydrogels in scavenging intracellular ROS was examined. Figure 5a, b reveal that cells cultured on PATA-based hydrogels experienced a reduction in ROS levels by over 60% relative to those in the control group. The assessment of the hypoglycemic efficacy of PATA-based hydrogels was conducted by measuring glucose levels in co-cultured cell culture supernatants using a glucose assay kit. As depicted in Fig. 5e, f, the PATA-GM (LP) and PATA-GM (SF/LP) groups demonstrated reduced glucose concentrations in the cell culture supernatants compared to the Control, PATA, and PATA-GM (SF) groups.

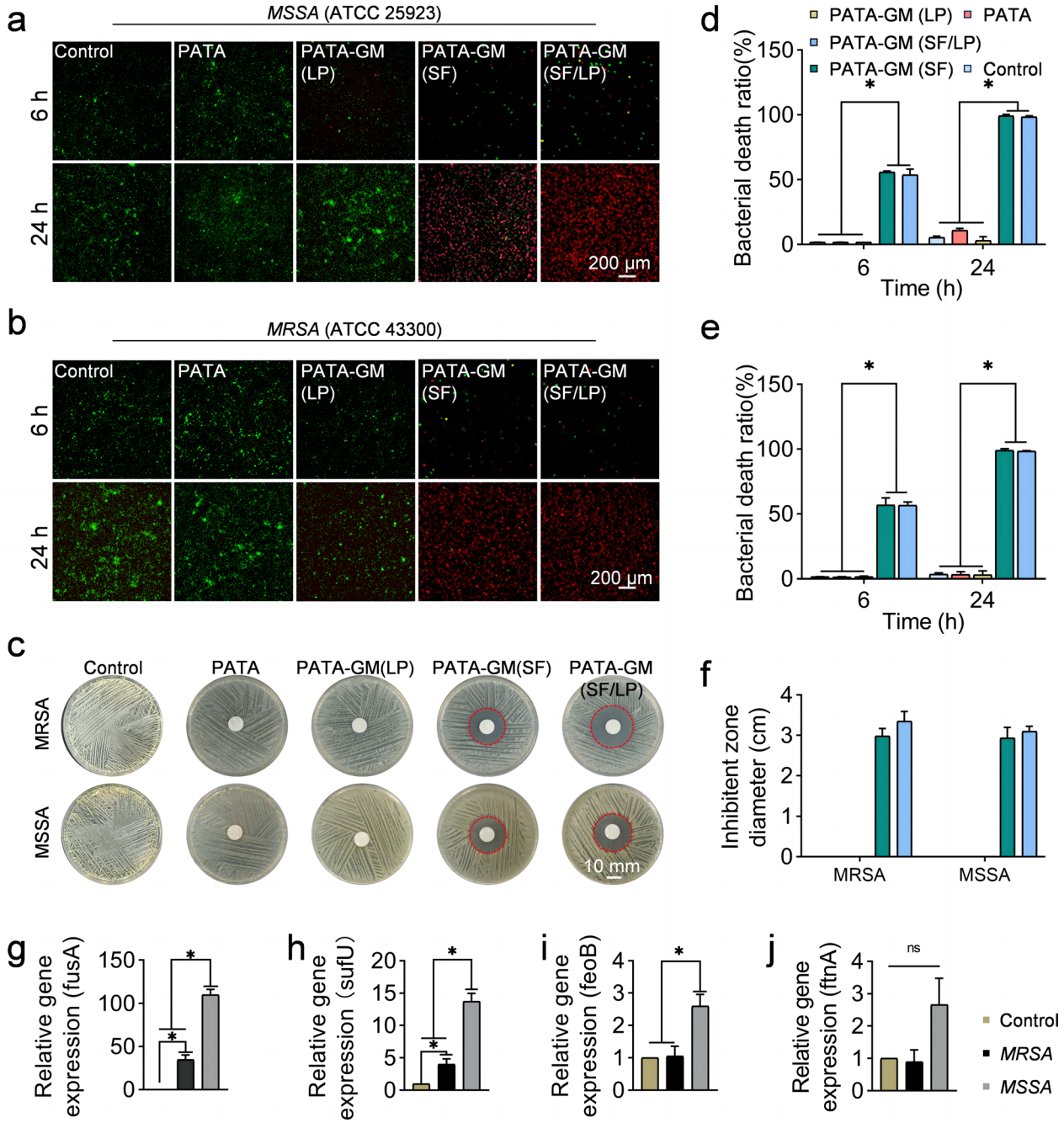

Fig. 4 Evaluation of the antibacterial efficacy of PATA-based hydrogels and Quantitative Real-Time PCR (qRT-PCR) analysis of antibacterial-relative gene expressions: **a**, **b** Visualization of live/dead bacterial (ATCC 25923 and ATCC 43300) interacting with PATA-based hydrogels at predetermined intervals; **c** Antibacterial efficacy of PATA-Based hydrogels demonstrated through inhibition zone assays on strains ATCC 25923 and ATCC 43300 cultured on agar plates; **d**, **e** Quantification of live/dead bacteria after exposure to hydrogels; **f** Quantitative assessment of inhibition zones; **g**–**j** qRT-PCR results analyzing gene expressions related to antibacterial activity; *$P < 0.05$

In vivo degradation, wound healing, antibacterial activity, and blood glucose regulation analysis

In vivo, the degradation of crosslinked hydrogel specimens was evaluated by implanting them under the skin and observing their degradation on days 1, 3, 5, 7, and 14, as shown in Fig. S11a. The hydrogels began to degrade from day 1 and were completely degraded by day 14, matching the skin healing rate in rats (Fig. S11c). To further evaluate the biocompatibility of the hydrogel, histological alterations in skin tissues adjacent to the hydrogel

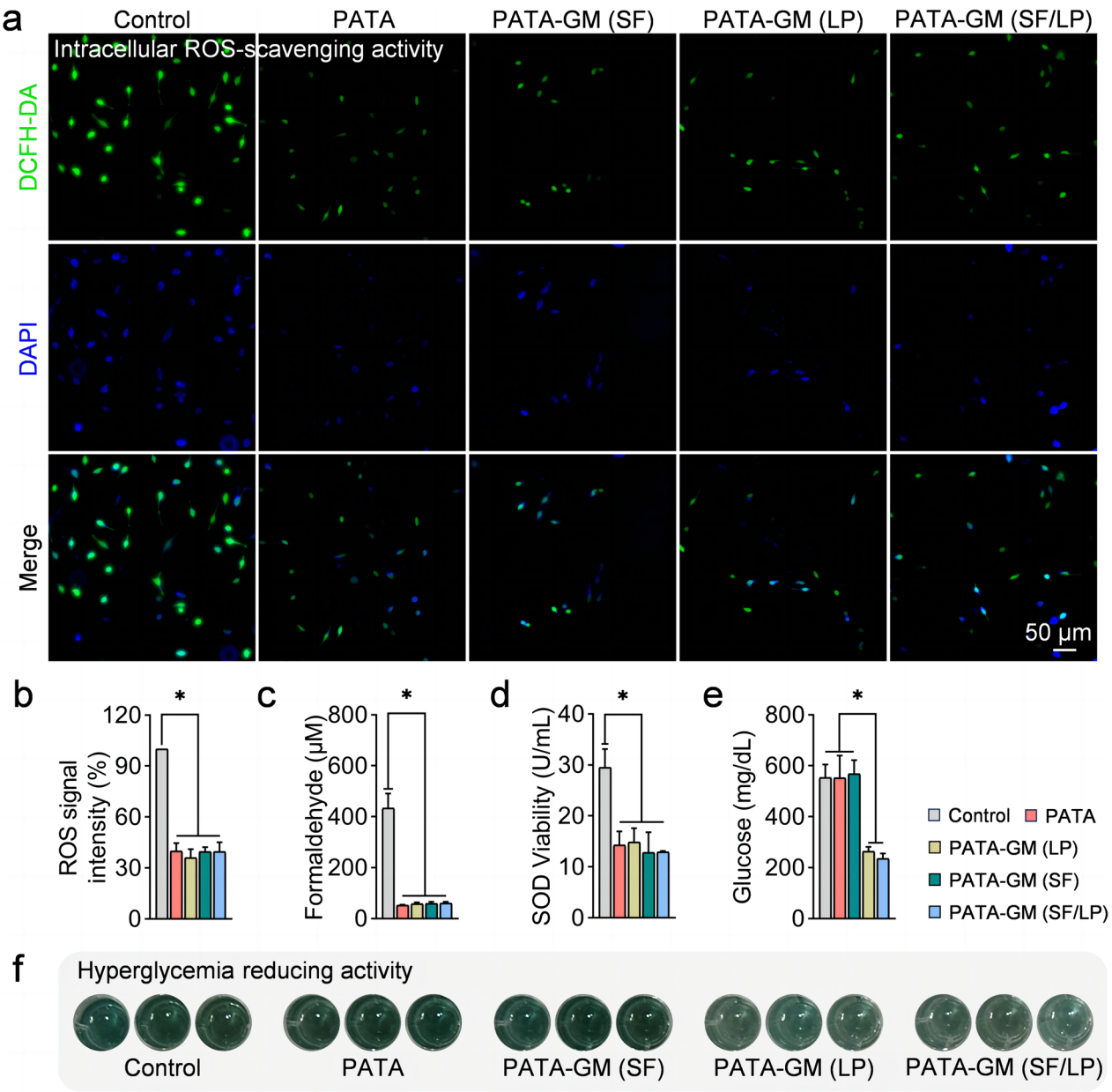

Fig. 5 Evaluation of ROS scavenging capabilities of PATA-based hydrogels in vitro: **a** Fluorescence microscopy images displaying ROS production (using DCFH-DA) in L929 cells incubated with PATA-based hydrogels post H_2O_2 exposure; **b** Quantification of ROS levels in L929 cells on PATA-based hydrogels following H_2O_2 treatment; **c** Analysis of SOD-like catalytic activity in hydrogels; **d** Results of CAT mimicry activity assays in PATA-based hydrogels; **e** Quantification of glucose concentrations in the supernatant of L929 cell cultures treated with PATA-based hydrogels; **f** Variations in colorimetric responses of L929 cell culture supernatants in 96-well plates following incubation with Glucose Assay Kit reagents. **P < 0.05*

were assessed using H&E and toluidine blue staining at 7 and 14 days after implantation. The results, depicted in Fig. S11b, showed negligible neutrophils and mast cells, crucial in inflammation, indicating the PATA-GM (SF/LP) hydrogel lacks of significant inflammatory response upon implantation. The in vivo antibacterial efficacy of the hydrogels was evaluated at 3 and 7 days post-surgery. As shown in Fig. S15a-b, the results indicated that SF-loaded hydrogels eradicated nearly 100% (> 99%) of the bacteria, compared to those without SF encapsulation. The rates of skin defect healing following treatment with various PATA-based hydrogel formulations were evaluated. The velocity of wound healing was quantified by comparing the current wound area as a percentage of the

original wound defect area, using a 15 mm inner diameter plastic circle for scale. Notably, the PATA-GM (SF/LP) group showed superior healing efficacy compared to the Control, PATA, PATA-GM (LP) and PATA-GM (SF) groups. Comparative analysis of wound dimensions and healing trajectories are elaborated in Fig. 6c, d. This study assessed the effect of topical MH application on blood glucose regulation in mice, with continuous monitoring during the subsequent experimental phase. Data revealed that blood glucose levels remained elevated for up to two days post-treatment. Conversely, in the MH-treated group, a significant reduction in blood glucose was observed after three days, as demonstrated in Fig. 6e. Groups not treated with MH exhibited blood glucose levels comparable to the control group. By the end of the monitoring period, the blood glucose of the group treated with MH was markedly lower than those in the MH-free group. Post the two-week experimental period, euthanasia was administered to the rats via pentobarbital overdose, followed by the collection of tissue specimens.

Histological, immunohistochemistry, and immunofluorescence analysis

Our study assessed the wound healing capabilities using Masson's trichrome and H&E staining, observed on days 7 and 14, detailed in Fig. 7a, b. The group treated with PATA-GM (SF/LP) dressing showcased superior healing compared to the Control, PATA, PATA-GM (LP), and PATA-GM (SF) groups, measured by the ratio of residual to initial wound areas. The PATA-GM (SF/LP) group exhibited the smallest scar width, depicted in Fig. 7c, d. Additional analysis of skin regeneration via H&E and Masson's trichrome staining (Fig. 7b) indicated the thinnest scar formation in the PATA-GM (SF/LP) group, with enhanced vascularization at the wound site (Fig. 7f). Furthermore, this treatment resulted in increased epidermal thickness relative to other groups (Fig. 7d), and a higher concentration of skin structures and blood vessels was observed in the PATA-GM (SF/LP) group (Fig. 7f). Corresponding with anti-infective and anti-ROS activity seen in vitro, these findings point to successful functional skin regeneration.

In the evaluation of neovascularization within wounds, CD31, indicative of vascular endothelial cells, and vascular endothelial growth factor (VEGF), essential for angiogenic processes, were employed for immunohistochemical analyses (Fig. S16 a-b, e–f). The results, illustrated in Fig. S16 a-b, revealed a significant formation of new blood vessels in both the PATA-GM (LP) and PATA-GM (SF/LP) treatment groups. Wounds treated with PATA-GM (SF/LP) exhibited a higher accumulation of native type I and type III collagen compared to those treated with PATA, PATA-GM (SF), PATA-GM (LP) or untreated skin, as shown in Fig. S16 c–d, g. Type I and III collagens, fundamental constituents of the dermal extracellular matrix (ECM), are recognized for their essential roles in the processes of wound healing and tissue remodeling. Immunostaining findings further substantiated the superiority of the PATA-GM (SF/LP) treatment. The expression levels of GLUT4 in diabetic wound tissues treated with PATA-based hydrogels were analyzed via immunofluorescence. Hydrogels loaded with MH exhibited elevated GLUT4 expression ($8.247 \pm 1.925\%$, $9.482 \pm 2.894\%$) compared to significantly lower levels in other groups ($0.205 \pm 0.148\%$, $0.668 \pm 0.174\%$, $0.770 \pm 0.319\%$).

Transcriptome sequencing analysis

Transcriptomic analyses were performed on RNA sequences from the dorsal skin tissues of rats subjected to a 3-day treatment with PATA-GM (SF/LP) versus control interventions. A total of 946 genes were sequenced. Of the differentially expressed genes (DEGs), 506 genes were found to be upregulated, and 443 were downregulated in the PATA-GM (SF/LP) treated group compared to the control (Fig. S17 a). Analysis of Kyoto Encyclopedia of Genes and Genomes (KEGG) pathways identified gene clusters associated with PPAR and Adipocytokine signaling pathways (Fig. 8a, b, d). Subsequent examination of DEGs between the PATA-GM (SF/LP) and control groups (Fig. 8e, f) revealed increased expression of genes facilitating glucose uptake, including glucose transporter 4 (Slc2a4), AMPK, PPARγ, and Adipoq, enhancing glucose transport and uptake (Fig. 8c). Additionally, qRT-PCR results indicated significant upregulation of Slc2a4, AMPK, PPARγ, and Adipoq gene expression in Rat-1 cells treated with MH-loaded PATA-based hydrogels compared to those treated with hydrogels without MH (Fig. 8g–j). Gene Ontology (GO) enrichment analysis underscored the DEGs' pivotal roles in essential biological processes, cellular component, and molecular function like "signaling receptor regulator activity", "extracellular region", and "sarcomere organization" (Fig. S17 c). Fig. S17 b showcases a heatmap of significantly altered DEGs.

Discussion

The increasing prevalence of diabetes worldwide brings forth significant clinical challenges in managing diabetic wounds. In response, a variety of biofunctional dressings have been developed to enhance the healing of these complex wounds. This research introduces an innovative multifunctional hydrogel dressing designed specifically for diabetic wound care. It comprises PVA and TSPBA, along with a dual-drug-loaded GM microgel. This GM

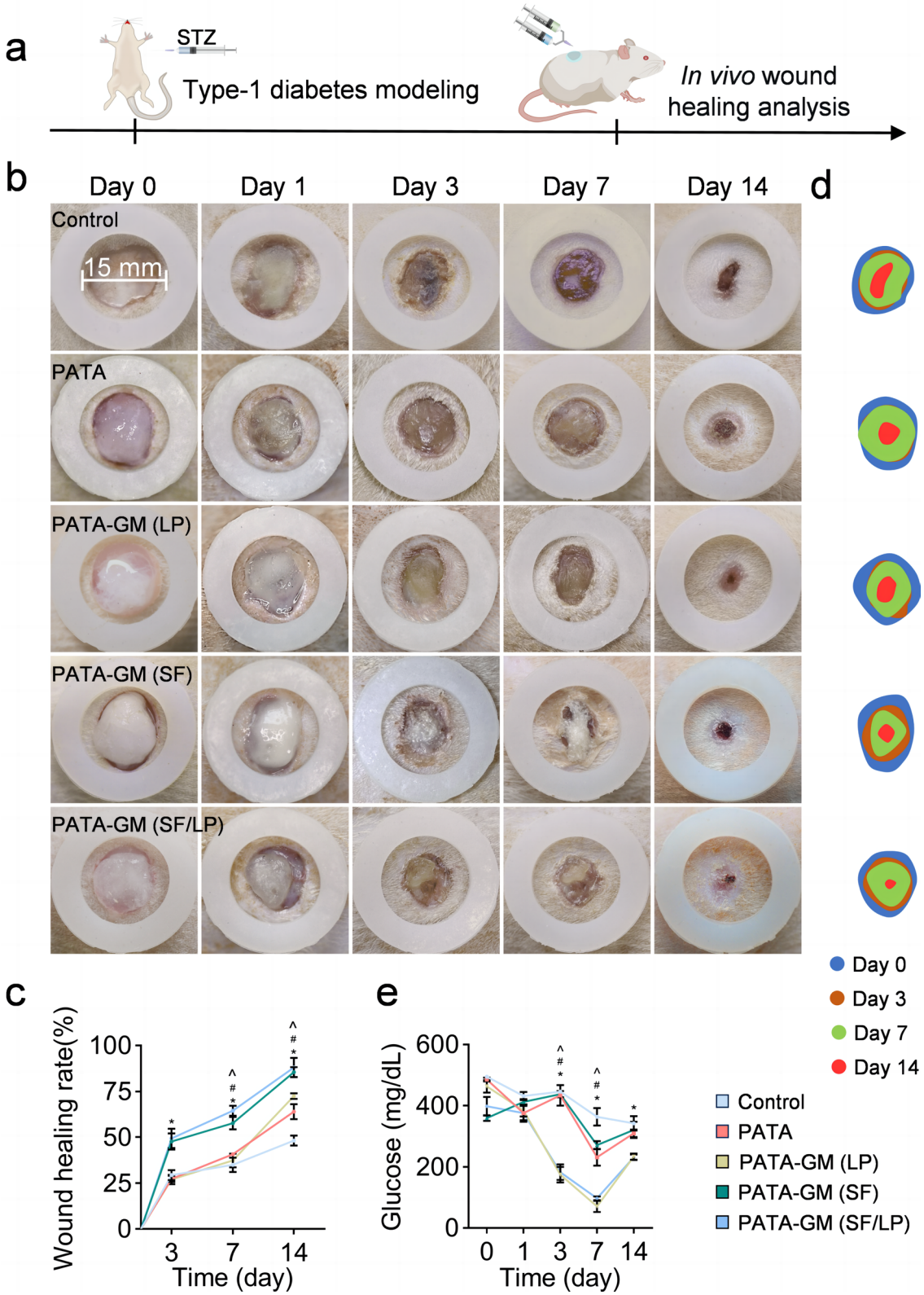

Fig. 6 Facilitation of infected diabetic wound healing by PATA-based hydrogels: **a** Diagrammatic representation of in vivo animal model experiments at various stages; **b**, **c** Images and quantitative evaluation of the wound healing process in Control, PATA, PATA-GM (SF), PATA-GM (LP), and PATA-GM (SF/LP) groups at predetermined intervals; **d** In vivo measurement of blood glucose levels; **e** Graphical representation of wound healing progression over a 14-day treatment period across the five experimental groups; $^{\#}P < 0.05$, $^{*}P < 0.05$

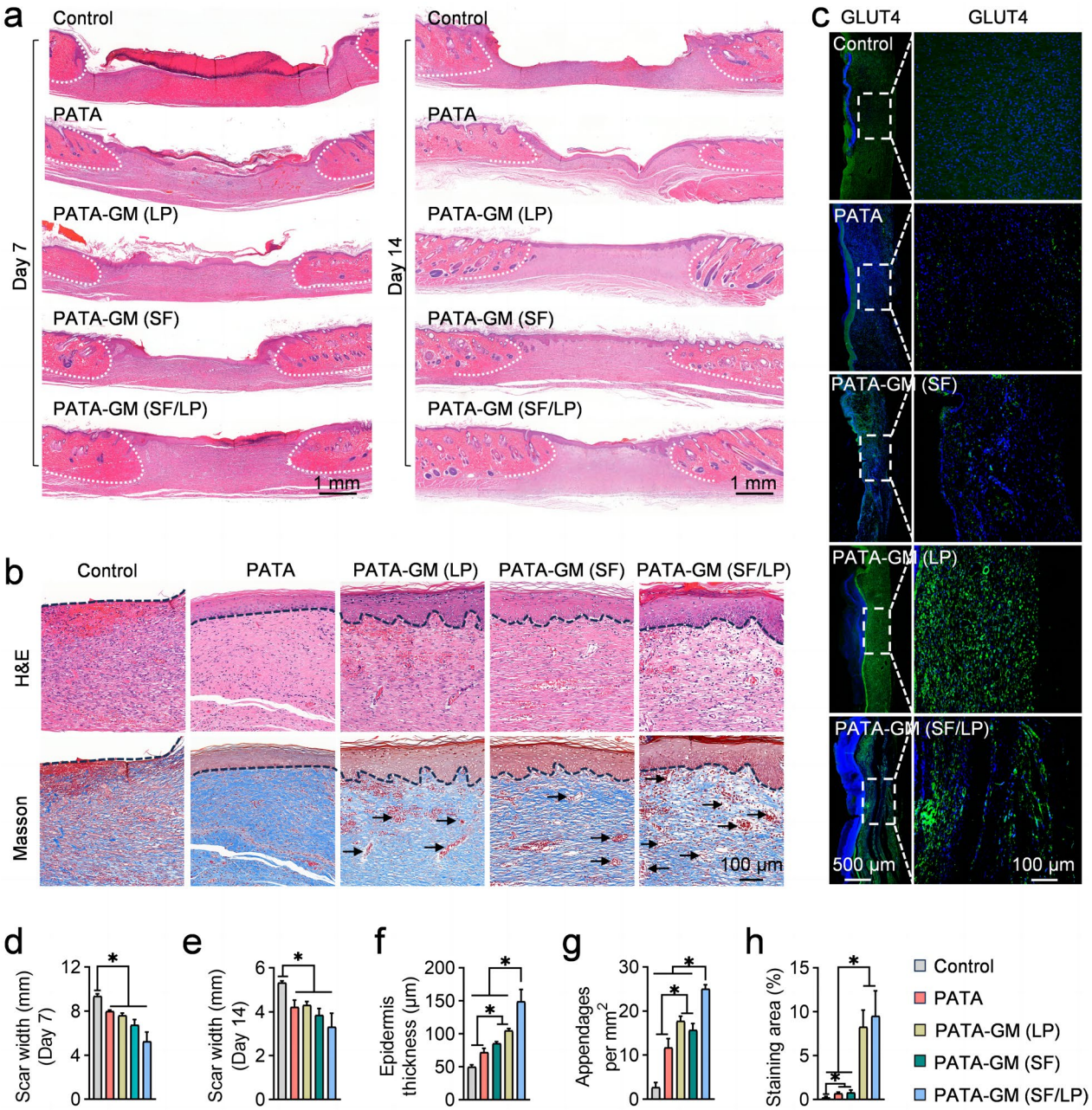

Fig. 7 Analysis of Wound Healing Using Histological Staining Techniques: **a** H&E stained sections of healed wounds, with incomplete healing areas marked by white dashed lines; **b** Detailed images of wounds stained with both H&E and Masson's trichrome, demarcating the epidermis with dashed black lines, whereas the blood vessels are indicated by black arrows; **c** High-resolution fluorescence microscopy images at 4 × and 20 × magnifications of wounds stained for Glut4 immunofluorescence analysis; **d**, **e** Measurement of scar width in wounds treated with various PATA-based hydrogels using Image J software (v1.53); **f** Determination of epidermal layer thickness in healed wounds treated with different PATA-based hydrogels using Image J software (v1.53); **g** Quantification and comparison of blood vessel count in wound regions treated with different hydrogels, analyzed using Image J software (v1.53); **h** Quantification of Glut4 immunofluorescence analysis in wounds treated with various PATA-based hydrogels using Image J software (v1.53); **P < 0.05*

microgel incorporates SF and LP encapsulating MH, aiming to optimize diabetic wound healing efficacy.

The SEM results illustrated in Fig. 2a(i–iii), display the physical integration of GM microgel within the PATA hydrogel. The synthesis of the injectable GM microgel-LP composite is further confirmed by LP staining, as depicted in Fig. 2a(iv), and FTIR analysis. This innovative system is engineered for dual functionality: to

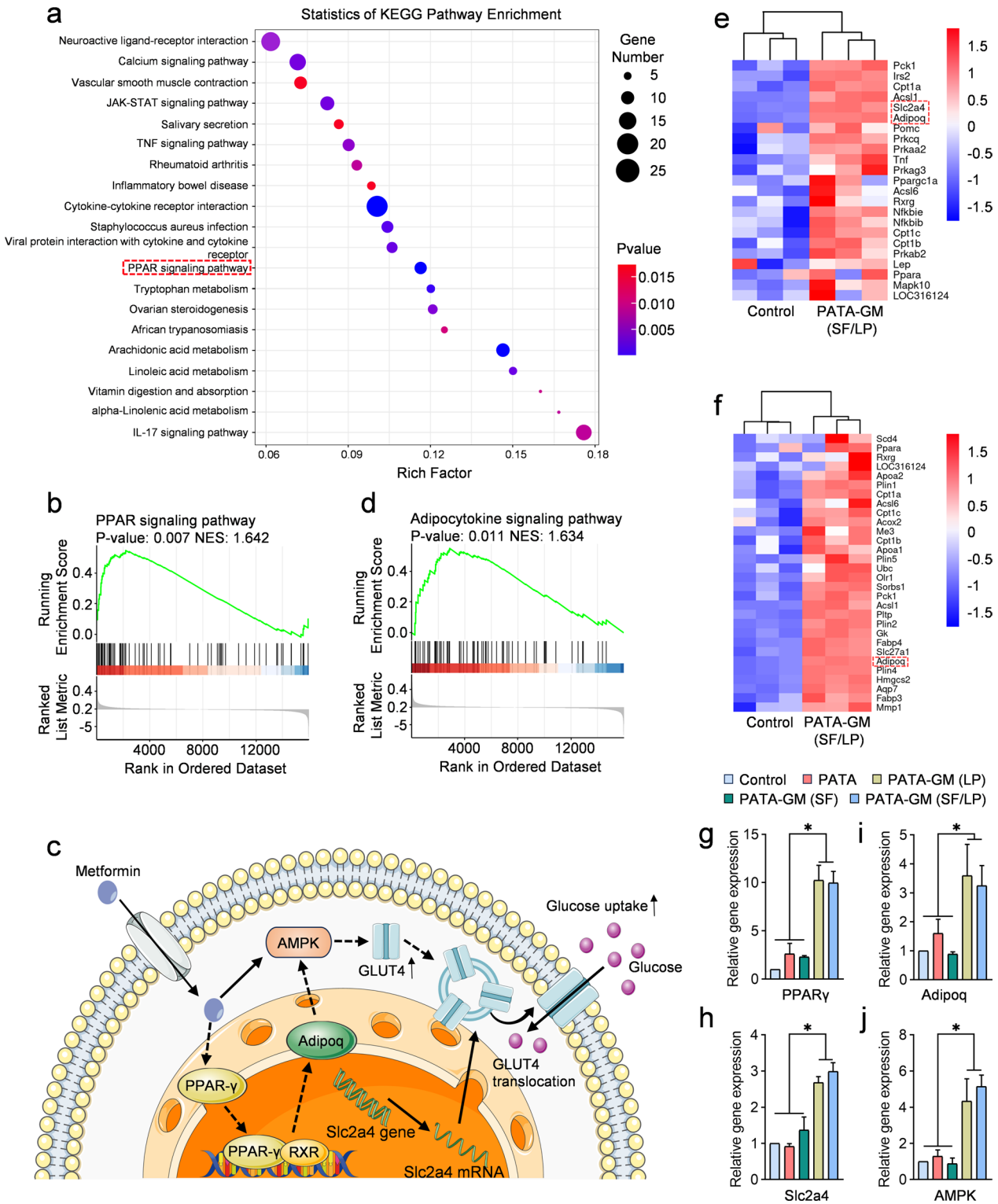

Fig. 8 Exploration of the in vivo effects of PATA-GM (SF/LP) treatment: **a** Evaluation of gene enrichment differences within the KEGG pathways; **b, d** Gene Set Enrichment Analysis (GSEA) illustrating differentially expressed genes in the KEGG pathways; **c** Mechanism of Metformin (MH) as hyperglycemia reducing agent; **e, f** Up-regulated genes associated with PPAR and Adipocytokine signaling pathways; **g**–**j** Analysis of glucose uptake-related gene expressions (Slc2a4, AMPK, PPARγ, and Adipoq) via qRT-PCR; **P < 0.05*

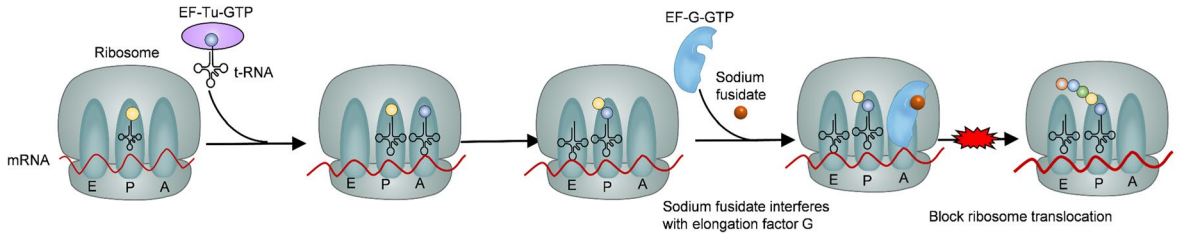

Fig. 9 Sodium fusidate (SF) bactericidal mechanism

concurrently administer antimicrobial agents and modulate glucose levels at the wound site, ensuring controlled release and targeted therapeutic action. FT-IR data, specifically the B-O stretching vibration at 1375 cm^{-1} shown in Fig. 2b, validate the synthesis of the PATA hydrogel through boronate esterification reactions between PVA and TSPBA. The formation of phenylboronic ester bonds within the hydrogel offers advantages over traditional crosslinking methods, including self-healing properties and environmental sensitivity, as demonstrated in Fig. 2g, h and Fig. S8. Traditional wound dressings often struggle with maintaining shape and adherence under mechanical stress [40]. In contrast, the PATA hydrogel adapts to the shape of the wound and adheres strongly, reducing the need for frequent dressing changes due to its enhanced adhesive properties (Fig. 2i, Fig. 6b). The hydrogel's ROS responsiveness is evident in Fig. 2g, where it shows rapid degradation in high-ROS environments and stability in low-ROS conditions. The susceptibility of boronic acid bonds to nucleophilic attacks, particularly by species such as H_2O_2, is attributed to the unique configuration of boron atoms within these bonds [41]. This characteristic facilitates responsive therapeutic agent delivery tailored to the complex microenvironment of the wound. In our study, borate ester linkages of the PATA hydrogel enable intelligent ROS scavenging at the wound site and precision-controlled release of encapsulated drugs in response to ROS levels (Fig. 2e, f). Drug release studies indicate that the PATA hydrogel discharges more medication in the presence of H_2O_2 (Fig. 2e, f), aligning with its degradation trend, while the incomplete release from GM microspheres is likely due to partial degradation and drug retention. Previous studies have investigated hydrogels loaded with SF or MH, and the release of SF and MH could last for 48 h and 10 days, respectively [42, 43]. In contrast, our findings demonstrate that the SF and MH components of our hydrogel system exhibit an extended-release profile, maintaining release over up to 15 days. This duration effectively spans the entire wound-healing process [44].

The biocompatibility of the newly designed wound dressing is crucial for its therapeutic effectiveness [45]. Our cytotoxicity tests reveal that L929 fibroblast bioactivity is preserved at SF and MH concentrations not exceeding 100 μg/mL and 10 mg/mL (Fig. 3a, Fig. S10). The uniform biocompatibility of PATA-based hydrogels, as evidenced by consistent fibroblast live cell ratio (Fig. 3b, f) and cell area (Fig. 3b, e), attests to their biosafety. Contrary to previous studies that questioned the safety of SF [46], we ascertain that its cytotoxic effects are primarily concentration-dependent. Enabled by controlled-release mechanisms, PATA hydrogels mitigate potential cytotoxicity due to drug build-up, corroborated by data presented in Fig. 3b, f. Encapsulating SF and MH within ideal concentration parameters appears to exert minimal impact on cellular viability, growth, and migratory behavior. The biocompatibility of the PATA-GM (SF/LP) hydrogels developed in this research was corroborated in vivo (Fig. S11), aligning with the outcomes of our in vitro assessments. The empirical evidence from both in vivo and in vitro analyses confirms the hydrogels' favorable biocompatibility and degradation properties.

The SF-loaded microgel within the hydrogel maintained bactericidal activity for up to 24 h, achieving a reduction of over 98% in ATCC 25923 (*MSSA*) and ATCC 43300 (*MRSA*) populations. The quaternary amine motifs in TSPBA may contribute to the minor increase in bacterial death ratio after 24 h in Fig. 4d, e; Fig. S13 a-b [47, 48]. SF-loaded hydrogels exhibited limited bactericidal activity against *E. coli* (Fig. S13a, b). This effectiveness is supported by inhibition zone, bacterial viability, and antibiofilm assay results, highlighting extensive antimicrobial potential of the hydrogel (Fig. 4). In comparison to other injectable hydrogels embedded with antimicrobial agents and electrospun fiber wound dressings, the material under investigation exhibited wider zones of inhibition, indicative of a more potent bactericidal effect [49, 50]. SF, targeting EF-G in staphylococci (Fig. 9), is effectively administered to the wound site via SF-loaded GM microgels. EF-G, a critical elongation factor, is pivotal in bacterial protein synthesis, specifically in the translational phase. The product of fusA gene, the EF-G protein, is vital for bacterial cell functionality. Research indicated that in ATCC 25923 (*MSSA*) and ATCC 43300 (*MRSA*), fusA is the gene encoding the EF-G protein [51]. In our investigation, PATA-GM (SF/LP)-treated bacterial

specimens underwent qRT-PCR assays. Figure 4g illustrates a marked elevation in the relative expression levels of the fusA gene compared to control groups, manifesting as a 109-fold increase in ATCC 25923 (*MSSA*) and a 34.9-fold increase in ATCC 43300 (*MRSA*). The mechanism of SF of action against bacterial proliferation is well-established [52, 53], operating through the inhibition of ribosomal function, specifically targeting the synthesis of the protein EF-G, encoded by the fusA gene in *S. aureus*. This inhibition by SF triggers a compensatory response in bacteria, leading to an upregulation of the fusA gene to counteract the suppression of EF-G synthesis, aligning with the observations in Fig. 4g. The resultant reduction in EF-G expression correlates with retardation of bacterial growth, potentially culminating in bacterial cell death. QRT-PCR analysis identified several genes integral to bacterial metabolism—sufU, feoB, fusD, ftnA, dnaK, and groL—among which sufU exhibited a notable increase in expression relative to others (Fig. 4h–j; Fig. S12e–g). SufU is implicated in the bacterial tricarboxylic acid (TCA) cycle [54], suggesting that its upregulation may serve as an adaptive response to the intracellular environmental perturbations induced by SF. Specifically, the expression of sufU was markedly higher in ATCC 25923 (*MSSA*) compared to ATCC 43300 (*MRSA*) (Fig. 4h). This differential expression extends to other genes associated with metabolic processes, including the stress response-related fusD, iron metabolism genes feoB and ftnA, and heat shock proteins dnaK and groL, all of which were significantly more expressed in ATCC 25923 (*MSSA*). The subdued response in ATCC 43300 (*MRSA*) could indicate a more stabilized metabolic state in these strains, potentially contributing to their reduced sensitivity to antibiotic interventions [55, 56].

ROS at physiological levels (1–10 nmol H_2O_2), play an essential role in normal wound healing by serving as an early defense mechanism, recruiting immune cells, and promoting endothelial cell proliferation. However, elevated ROS levels exceeding physiological norms (>100 nmol H_2O_2) can cause oxidative stress, damaging essential biomolecules like DNA, RNA, and enzymes, and consequently hindering the healing process [57]. Figure 5 presents the ROS scavenging efficacy of the PATA-based hydrogel. This hydrogel demonstrates a dual action, effectively reducing both extracellular (Fig. 5a, b) and intracellular ROS levels (Fig. 5c, d), as evidenced by its comparison with the control group. The observed ROS neutralization is attributed to the borate ester bonds within the hydrogel, which actively consume extracellular ROS and concurrently alleviate intracellular oxidative stress. The antioxidant properties structure of borate ester effectively neutralizes reactive oxygen species (ROS), thereby diminishing their overall concentration [58]. Additionally, the borate ester bonds potentially modulate mitochondrial function and NADPH oxidase activity, further curtailing ROS generation [59].

Bactericidal, ROS scavenging, and glycemic control ability were further evaluated using a type-I diabetic infected wound model in SD rats (Fig. 6a). Figures 6b–d, 7a shows that rats treated with PATA-GM (SF/LP) exhibit the fastest wound closure. In Fig. 6b, rats receiving MH-loaded PATA hydrogel treatment exhibited effective glucose regulation on days 3 and 7, with a subsequent incremental rise in blood glucose levels. This pattern aligns with MH release dynamics presented in Fig. 2f. Significantly, on day 14, these MH-treated rats demonstrated reduced blood glucose levels compared to their untreated counterparts. Research indicates that the topical administration of MH is effective in managing blood glucose [44]. Furthermore, compared with the blood glucose level in the control group (342.61 ± 24.141 mg/dL), the PATA and PATA-GM (SF) groups exhibited lower values (309.31 ± 12.246 mg/dL and 321.32 ± 27.286 mg/dL, respectively) (Fig. 6e). This reduction is likely due to glucose binding with boronic acid, which may contribute to glucose regulation and controlled drug release in the treatment of diabetic wounds [60–62]. While local antidiabetic agents, such as insulin, offer some benefits [63], our study highlights the superior efficacy of the MH-loaded hydrogel in sustaining blood glucose reduction. Compared with the exclusive use of local antidiabetic agents such as insulin in topical treatments fails to maintain prolonged blood glucose reduction due to the transient efficacy of insulin [64]. The novel system introduced in this study distinguishes itself by exhibiting a more rapid and consistent glucose regulation, achieving a significant reduction in blood glucose levels in rats between days 3 and 7 (Fig. 6d). The findings demonstrate that the injectable hydrogel/microgel system, enriched with MH, supports the sustained modulation of blood glucose concentrations. This effect is attributed to the incorporation of LP into microgels, which initiates hydrogen bond interactions among these components, thus ensuring stable and continuous dissemination of the encapsulated therapeutic agents [65, 66].

Moreover, transcriptomic analyses of tissue samples from rats administered with PATA-GM (SF/LP) hydrogel reveal its efficacy in diabetic wound healing. Transcriptomic sequencing KEGG pathway statistics revealed a significant enrichment of the PPAR signaling pathway (Fig. 8a). Notably, MH treatment led to an augmented expression of PPARγ, a pivotal gene within the PPAR cascade, which in turn facilitated the upregulation of Adipoq gene expression (Fig. 8c) [67, 68]. This regulatory mechanism is essential for the activation of the Adipocytokine signaling pathway (Fig. 8b, d, e–f) [69] Extant literature

confirms that the enhancement of PPARγ expression within the PPAR signaling framework is instrumental in activating AMPK, a crucial modulator of the Adipocytokine signaling pathway [70]. Consequently, AMPK activation boosts the expression of the Slc2a4 gene, which plays a key role in modulating GLUT4 dynamics (Fig. 8c), thereby augmenting GLUT4 expression and its translocation to the cellular membrane [71]. The phosphorylation and subsequent activation of AMPK are fundamental processes underlying the broad-spectrum effects of metformin, especially regarding the translocation of GLUT4 [72]. Immunofluorescence imaging presented in Fig. 7c reveals a significant augmentation in GLUT4 expression post-treatment with MH-loaded nanoliposomes, a finding that is consistent with transcriptomic sequencing data and the results of qRT-PCR analyses. The results indicate that the MH-loaded hydrogel significantly enhances GLUT4 expression, thereby augmenting local glucose absorption and effectively modifying the high-glucose microenvironment of the wound. In our Transcriptomic sequencing results, Gene Ontology (GO) enrichment analysis further highlighted the critical functions of DEGs in key biological processes, cellular component, and molecular function notably "signaling receptor regulator activity", "extracellular region", and "sarcomere organization" (Fig. S17c) [73–75].

To evaluate the caliber of tissue repair, H&E, and Masson's trichrome staining were utilized (Fig. 7). The wounds subjected to PATA-GM (SF/LP) treatment displayed the narrowest scar width. The wounds subjected to PATA-GM (SF/LP) treatment displayed the narrowest scar width. Moreover, treatment modalities enriched with MH resulted in wounds with enhanced epidermal thickness, type 1 and type 3 collagen expression (Fig. 7a, b; Fig. S16 c-d, g). In comparison to our prior studies [76] which focused solely on ROS elimination and antibacterial properties, the controlled-release formulation of PATA-GM (SF/LP) demonstrates a more profound capacity to expedite the healing of diabetic wounds. MH not only enhanced collagen expression and epidermal thickness, but also increased wound vascular endothelial growth factor (VEGF) expression and blood vessel number (Fig. S16a, b). To investigate the underlying mechanisms facilitating angiogenesis, immunohistochemical assays were conducted to evaluate VEGF and CD31 expression levels. CD31 is identified as a biomarker for vascular endothelial cells, whereas VEGF is essential for angiogenic processes. Results depicted in Fig. S16a, b, e–f indicate that PATA-GM (SF/LP) administration significantly enhances the expression of CD31 and VEGF. VEGF engages in the activation of downstream signaling cascades, including the PI3K-Akt and MAPK pathways [77], via interaction with vascular endothelial growth factor receptor (VEGFR), which are critical for cellular proliferation, migration, and survival [78]. In comparison to existing literature [79, 80], our multifunctional hydrogel more effectively enhances the expression of VEGF and CD31. The incorporation of MH not only promotes vascularization but also better facilitates the increased accumulation of types I and III collagen at the wound site, indicative of progressive tissue reconstruction.

PATA hydrogel, notable for its injectability, enhanced adhesive, and self-healing properties, adheres effectively to irregular wound shapes. It remains in place despite wound deformation and movements of the subject, as shown in Fig. S6, Fig. 2h, i, and Fig. 6b. This is attributed to the formation of boronate bonds within PATA, specifically between TSPBA and hydroxyl groups (-OH) on the object's surface. Additionally, the hydrogen bonds formed between PVA and functional groups on the surface, such as amino groups ($-NH_2$) and hydroxyl groups (-OH), further bolster the adhesiveness of the hydrogel.

The PATA-GM (SF/LP) hydrogel demonstrates remarkable proficiency in treating infections, modulating the local microenvironment, and managing blood glucose levels. Comprehensive in vivo and in vitro analyses have validated its capability for responsive release on demand, reducing the necessity for frequent dressing changes. The hydrogel effectively combats infection, scavenges ROS, and regulates blood glucose in diabetic wounds, thereby expediting wound healing and skin regeneration processes.

Conclusion

This study introduces an injectable PATA hydrogel, incorporating SF-loaded microgel and MH-loaded nanoliposomes, devised as an all-encompassing wound care solution. Its efficacy in delivering antimicrobial activity, neutralizing ROS, regulating blood glucose, and providing robust adherence is substantiated by comprehensive in vitro and in vivo studies. Notably effective under conditions of infection, hyperglycemia, and high ROS, the hydrogel dressing expedites wound closure and promotes dermal regeneration, leveraging the synergistic effects of SF, borate ester bonds, and MH. This novel wound dressing combines critical properties, including antimicrobial, ROS mitigation, glucose management, and adhesion, enhanced by a streamlined manufacturing process that enhances its viability for clinical use.

Abbreviations

DW	Diabetic wounds
PVA	Poly (vinyl alcohol)
MSSA	*Staphylococcus aureus*
MRSA	Methicillin-resistant *Staphylococcus aureus*
DAPI	4′,6-Diamidino-2-phenylindole
SD	Sprague–Dawley

FT-IR	Fourier-transform infrared spectroscopy
SEM	Scanning electron microscopy
ROS	Reactive oxygen species
SF	Sodium fusidate
MH	Metformin hydrochloride
PVA	Polyvinyl alcohol
TSPBA	N1-(4-boronobenzyl)-N3-(4-boronophenyl)-N1, N1, N3, N3-tetramethylpropane-1, 3-diaminium
GM	Gelatin methacryloyl
LP	Nanoliposomes
EF-G	Elongation factor G
UV	Ultraviolet
H_2O_2	Hydrogen peroxide
KBr	Potassium bromide
mM	mmol/L
μM	μmol/L
SOD	Superoxide dismutase
CAT	Catalase
MDH	Multifunctional dressings

Supplementary Information

The online version contains supplementary material available at https://doi.org/10.1186/s12951-024-02687-y.

Additional file 1.

Acknowledgements
Not applicable.

Author contributions
R.C. contributed to the conceptualization, methodology, and writing of the original draft. P.W. and J.X. contributed to data curation and software. Z.T., J.F., Y.N. contributed to visualization and investigation. Q.Z., D.W., M.L., H.M., H.L. contributed to software and validation. H.C. was involved in writing-reviewing and editing. Z.S. and J.W. contributed to supervision. All authors read and approved the final manuscript.

Funding
This study was funded by the National Natural Science Foundation of China (82272463, 82272514).

Data availability
All data generated or analyzed during this study are included in this published article.

Declarations

Ethics approval and consent to participate
All husbandry and animal methodologies conformed to the ethical standards stipulated in the National Research Council's Guide for the Care and Use of Laboratory Animals and were approved by the Animal Ethics Committee of Southern Medical University, ensuring humane practices in animal handling.

Consent for publication
All authors agree to be published.

Competing interests
The authors declare that they have no known competing financial interests or personal relationships that could have appeared to influence the work reported in this paper.

Author details
[1]Department of Orthopedic, Nanfang Hospital, Southern Medical University, Guangzhou 510515, China. [2]Department of Orthopedics, The Second Affiliated Hospital of Nanchang University, Jiangxi Medical College, Nanchang University, Nanchang 330006, China.

Received: 10 April 2024 Accepted: 1 July 2024
Published online: 27 July 2024

References

1. Patel S, Srivastava S, Singh MR, Singh D. Mechanistic insight into diabetic wounds: pathogenesis, molecular targets and treatment strategies to pace wound healing. Biomed Pharmacother. 2019;112: 108615.
2. Zhao H, Huang J, Li Y, Lv X, Zhou H, Wang H, Xu Y, Wang C, Wang J, Liu Z. ROS-scavenging hydrogel to promote healing of bacteria infected diabetic wounds. Biomaterials. 2020;258: 120286.
3. Wang S, Zheng H, Zhou L, Cheng F, Liu Z, Zhang H, Wang L, Zhang Q. Nanoenzyme-reinforced injectable hydrogel for healing diabetic wounds infected with multidrug resistant bacteria. Nano Lett. 2020;20:5149–58.
4. Zhang S, Ge G, Qin Y, Li W, Dong J, Mei J, Ma R, Zhang X, Bai J, Zhu C, et al. Recent advances in responsive hydrogels for diabetic wound healing. Mater Today Bio. 2023;18: 100508.
5. Chu X, Xiong Y, Knoedler S, Lu L, Panayi AC, Alfertshofer M, Jiang D, Rinkevich Y, Lin Z, Zhao Z, et al. Immunomodulatory nanosystems: advanced delivery tools for treating chronic wounds. Research. 2023;6:0198.
6. Liang Y, Li M, Yang Y, Qiao L, Xu H, Guo B. pH/glucose dual responsive metformin release hydrogel dressings with adhesion and self-healing via dual-dynamic bonding for athletic diabetic foot wound healing. ACS Nano. 2022;16:3194–207.
7. Li Y-J, Wei S-C, Chu H-W, Jian H-J, Anand A, Nain A, Huang Y-F, Chang H-T, Huang C-C, Lai J-Y. Poly-quercetin-based nanoVelcro as a multifunctional wound dressing for effective treatment of chronic wound infections. Chem Eng J. 2022;437: 135315.
8. Jia B, Li G, Cao E, Luo J, Zhao X, Huang H. Recent progress of antibacterial hydrogels in wound dressings. Mater Today Bio. 2023;19: 100582.
9. Yang C-J, Nguyen DD, Lai J-Y. Poly(l-Histidine)-mediated on-demand therapeutic delivery of roughened ceria nanocages for treatment of chemical eye injury. Adv Sci. 2023;10:2302174.
10. Jian H-J, Anand A, Lai J-Y, Unnikrishnan B, Chang H-T, Harroun SG, Huang C-C. In situ hybridization of polymeric curcumin to arginine-derived carbon quantum dots for synergistic treatment of bacterial infections. ACS Appl Mater Interfaces. 2023;15:26457–71.
11. Ali Zahid A, Chakraborty A, Shamiya Y, Ravi SP, Paul A. Leveraging the advancements in functional biomaterials and scaffold fabrication technologies for chronic wound healing applications. Mater Horiz. 2022;9:1850–65.
12. Yang J, Huang Z, Tan J, Pan J, Chen S, Wan W. Copper ion/gallic acid MOFs-laden adhesive pomelo peel sponge effectively treats biofilm-infected skin wounds and improves healing quality. Bioactive Mater. 2024;32:260–76.
13. Wang C, Wang J, Zhang X, Yu S, Wen D, Hu Q, Ye Y, Bomba H, Hu X, Liu Z, et al. In situ formed reactive oxygen species–responsive scaffold with gemcitabine and checkpoint inhibitor for combination therapy. Sci Transl Med. 2018;10:eaan3682.
14. Khorsandi K, Hosseinzadeh R, Esfahani H, Zandsalimi K, Shahidi FK, Abrahamse H. Accelerating skin regeneration and wound healing by controlled ROS from photodynamic treatment. Inflamm Regener. 2022;42:40.
15. Marco-Dufort B, Tibbitt MW. Design of moldable hydrogels for biomedical applications using dynamic covalent boronic esters. Mater Today Chem. 2019;12:16–33.
16. Li D, Chen K, Tang H, Hu S, Xin L, Jing X, He Q, Wang S, Song J, Mei L, et al. A logic-based diagnostic and therapeutic hydrogel with multistimuli responsiveness to orchestrate diabetic bone regeneration. Adv Mater. 2022;34:2108430.
17. Yang J, Zhu Y, Wang F, Deng L, Xu X, Cui W. Microfluidic liposomes-anchored microgels as extended delivery platform for treatment of osteoarthritis. Chem Eng J. 2020;400: 126004.
18. Zhou C, Cao Y, Liu C, Guo W. Microparticles by microfluidic lithography. Mater Today. 2023;67:178–202.
19. Zhang C, Grossier R, Candoni N, Veesler S. Preparation of alginate hydrogel microparticles by gelation introducing cross-linkers using droplet-based microfluidics: a review of methods. Biomater Res. 2021;25:41.
20. Sun X, Agate S, Salem KS, Lucia L, Pal L. Hydrogel-based sensor networks: compositions, properties, and applications—a review. ACS Appl Bio Mater. 2021;4:140–62.

21. Dong R, Liu Y, Mou L, Deng J, Jiang X. Microfluidics-based biomaterials and biodevices. Adv Mater. 2019;31:1805033.
22. Eid AM, Istateyeh I, Salhi N, Istateyeh T. Antibacterial activity of fusidic acid and sodium fusidate nanoparticles incorporated in pine oil nanoemulgel. Int J Nanomed. 2019;14:9411–21.
23. Tomlinson JH, Kalverda AP, Calabrese AN. Fusidic acid resistance through changes in the dynamics of the drug target. Proc Natl Acad Sci. 2020;117:25523–31.
24. Kittel Y, Kuehne AJC, De Laporte L. Translating therapeutic microgels into clinical applications. Adv Healthc Mater. 2022;11:2101989.
25. Nguyen DD, Luo L-J, Yang C-J, Lai J-Y. Highly retina-permeating and long-acting resveratrol/metformin nanotherapeutics for enhanced treatment of macular degeneration. ACS Nano. 2023;17:168–83.
26. Luo L-J, Jian H-J, Harroun SG, Lai J-Y, Unnikrishnan B, Huang C-C. Targeting nanocomposites with anti-oxidative/inflammatory/angiogenic activities for synergistically alleviating macular degeneration. Appl Mater Today. 2021;24: 101156.
27. Tasharrofi N, Nourozi M, Marzban A. How liposomes pave the way for ocular drug delivery after topical administration. J Drug Delivery Sci Technol. 2022;67: 103045.
28. Large DE, Abdelmessih RG, Fink EA, Auguste DT. Liposome composition in drug delivery design, synthesis, characterization, and clinical application. Adv Drug Deliv Rev. 2021;176: 113851.
29. He Y, Sun M, Wang J, Yang X, Lin C, Ge L, Ying C, Xu K, Liu A, Wu L. Chondroitin sulfate microspheres anchored with drug-loaded liposomes play a dual antioxidant role in the treatment of osteoarthritis. Acta Biomater. 2022;151:512–27.
30. Thompson AK, Mozafari MR, Singh H. The properties of liposomes produced from milk fat globule membrane material using different techniques. Lait. 2007;87:349–60.
31. Shi Z, Zhong Q, Chen YH, Gao J, Pan X, Lian Q, Chen R, Wang PK, Wang J, Shi ZJ, Cheng H. Nanohydroxyapatite, nanosilicate-reinforced injectable, and biomimetic gelatin-methacryloyl hydrogel for bone tissue engineering. Int J Nanomed. 2021;16:5603–19.
32. Li ZH, Zhu DS, Hui Q, Bi JN, Yu BJ, Huang Z, Hu SQ, Wang ZZ, Caranasos T, Rossi J, et al. Injection of ROS-responsive hydrogel loaded with basic fibroblast growth factor into the pericardial cavity for heart repair. Adv Func Mater. 2021;31:10.
33. Wang JQ, Ye YQ, Yu JC, Kahkoska AR, Zhang XD, Wang C, Sun WJ, Corder RD, Chen ZW, Khan SA, et al. Core-shell microneedle gel for self-regulated insulin delivery. ACS Nano. 2018;12:2466–73.
34. Hu JJ, Yu XZ, Zhang SQ, Zhang YX, Chen XL, Long ZJ, Hu HZ, Xie DH, Zhang WH, Chen JX, Zhang Q. Hydrogel with ROS scavenging effect encapsulates BR@Zn-BTB nanoparticles for accelerating diabetic mice wound healing via multimodal therapy. Iscience. 2023;26:23.
35. Zhu W, Mei J, Zhang X, Zhou J, Xu D, Su Z, Fang S, Wang J, Zhang X, Zhu C. Photothermal nanozyme-based microneedle patch against refractory bacterial biofilm infection via iron-actuated janus ion therapy. Adv Mater. 2022;34:2207961.
36. Chen W, Zheng D, Chen H, Ye T, Liu Z, Qi J, Shen H, Ruan H, Cui W, Deng L. Circadian clock regulation via biomaterials for nucleus pulposus. Adv Mater. 2023;35:2301037.
37. Gao T, Xu G, Ma T, Lu X, Chen K, Luo H, Chen G, Song J, Ma X, Fu W, et al. ROS-responsive injectable hydrogel loaded with SLC7A11-modRNA inhibits ferroptosis and mitigates intervertebral disc degeneration in rats. Adv Healthc Mater. 2401103.
38. Morey M, Srivastava A, Pandit A. Glucose-responsive gene delivery at physiological ph through tertiary-amine stabilized boronate-PVA particles synthesized by one-pot reaction. Pharmaceutics. 2021;13:10.
39. Cascioferro S, Carbone D, Parrino B, Pecoraro C, Giovannetti E, Cirrincione G, Diana P. Therapeutic strategies to counteract antibiotic resistance in MRSA biofilm-associated infections. ChemMedChem. 2021;16:65–80.
40. Zou CY, Lei XX, Hu JJ, Jiang YL, Li QJ, Song YT, Zhang QY, Li-Ling J, Xie HQ. Multi-crosslinking hydrogels with robust bio-adhesion and pro-coagulant activity for first-aid hemostasis and infected wound healing. Bioactive Materials. 2022;16:388–402.
41. Yu J, Zhang RL, Chen BH, Liu XL, Jia Q, Wang XF, Yang Z, Ning PB, Wang ZL, Yang Y. Injectable reactive oxygen species-responsive hydrogel dressing with sustained nitric oxide release for bacterial ablation and wound healing. Adv Func Mater. 2022;32:11.
42. Ullah N, Khan D, Ahmed N, Zafar A, Shah KU, ur Rehman A. Lipase-sensitive fusidic acid polymeric nanoparticles based hydrogel for on-demand delivery against MRSA-infected burn wounds. J Drug Delivery Sci Technol. 2023;80:14.
43. Zheng DD, Chen W, Ruan HT, Cai ZW, Chen XY, Chen TT, Zhang YH, Cui WG, Chen H, Shen HX. Metformin-hydrogel with glucose responsiveness for chronic inflammatory suppression. Chem Eng J. 2022;428:12.
44. Zhang WR, Yang Z, Zhang MZ, He JL, Li SZ, Sun XW, Ni PH. A hybrid hydrogel constructed using drug loaded mesoporous silica and multiple response copolymer as an intelligent dressing for wound healing of diabetic foot ulcers. J Mater Chem B. 2023;11:4922–33.
45. Luo L-J, Nguyen DD, Huang C-C, Lai J-Y. Therapeutic hydrogel sheets programmed with multistage drug delivery for effective treatment of corneal abrasion. Chem Eng J. 2022;429: 132409.
46. Kraus CN, Burnstead BW. The safety record of fusidic acid in Non-US markets: a focus on skin infections. Clin Infect Dis. 2011;52:S527–37.
47. Jiao Y, Niu LN, Ma S, Li J, Tay FR, Chen JH. Quaternary ammonium-based biomedical materials: state-of-the-art, toxicological aspects and antimicrobial resistance. Prog Polym Sci. 2017;71:53–90.
48. Wang S, Wu W-Y, Yeo JCC, Soo XYD, Thitsartarn W, Liu S, Tan BH, Suwardi A, Li Z, Zhu Q, Loh XJ. Responsive hydrogel dressings for intelligent wound management. BMEMat. 2023;1: e12021.
49. Mabroum H, Elbaza H, Ben Youcef H, Oudadesse H, Noukrati H, Barroug A. Design of antibacterial apatitic composite cement loaded with Ciprofloxacin: investigations on the physicochemical Properties, release Kinetics, and antibacterial activity. Int J Pharm. 2023;637: 122861.
50. Adeli H, Khorasani MT, Parvazinia M. Wound dressing based on electrospun PVA/chitosan/starch nanofibrous mats: fabrication, antibacterial and cytocompatibility evaluation and in vitro healing assay. Int J Biol Macromol. 2019;122:238–54.
51. Singh A, Singh K, Sharma A, Kaur J, Kaur R, Kaur J, Kaur K, Chadha R, Bedi PMS. Rational utilization of 1,2,3-triazole scaffold in anti-MRSA drug development: design strategies, structural insights and pharmacological outcomes. J Mol Struct. 2024;1295:23.
52. Huang X, Shen QK, Guo HY, Quan ZS, Li XT. Research, development and pharmacological activity of fusidic acid and its derivatives. J Mol Struct. 2023;1291:29.
53. Chung PY. Novel targets of pentacyclic triterpenoids in *Staphylococcus aureus*: a systematic review. Phytomedicine. 2020;73:9.
54. Das M, Sreedharan S, Shee S, Malhotra N, Nandy M, Banerjee U, Kohli S, Rajmani RS, Chandra N, Seshasayee ASN, et al. Cysteine desulfurase (IscS)-mediated fine-tuning of bioenergetics and SUF expression prevents *Mycobacterium tuberculosis* hypervirulence. Sci Adv. 2023;9:21.
55. Kumar V, Yasmeen N, Pandey A, Chaudhary AA, Alawam AS, Rudayni HA, Islam A, Lakhawat SS, Sharma PK, Shahid M. Antibiotic adjuvants: synergistic tool to combat multi-drug resistant pathogens. Front Cell Infect Microbiol. 2023;13:14.
56. Ahmed S, Ahmed MZ, Rafique S, Almasoudi SE, Shah M, Jalil NAC, Ojha SC. Recent approaches for downplaying antibiotic resistance: molecular mechanisms. Biomed Res Int. 2023;2023:27.
57. Liu TF, Xiao BW, Xiang F, Tan JL, Chen Z, Zhang XR, Wu CZ, Mao ZW, Luo GX, Chen XY, Deng J. Ultrasmall copper-based nanoparticles for reactive oxygen species scavenging and alleviation of inflammation related diseases. Nat Commun. 2020;11:16.
58. Zhang TH, Chen X, Xiao CS, Zhuang XL, Chen XS. Synthesis of a phenylboronic ester-linked PEG-lipid conjugate for ROS-responsive drug delivery. Polym Chem. 2017;8:6209–16.
59. Gatin-Fraudet B, Ottenwelter R, Le Saux T, Norsikian S, Pucher M, Lombes T, Baron A, Durand P, Doisneau G, Bourdreux Y, et al. Evaluation of borinic acids as new, fast hydrogen peroxide-responsive triggers. Proc Natl Acad Sci USA. 2021;118: e2107503118.
60. GhavamiNejad A, Lu B, Giacca A, Wu XY. Glucose regulation by modified boronic acid-sulfobetaine zwitterionic nanogels—a non-hormonal strategy for the potential treatment of hyperglycemia. Nanoscale. 2019;11:10167–71.
61. Xiao Y, Zhang J, Wu T, Chen S, Huang Z, Du J. Three-day blood glucose control via a glucose modulator of glycopolymersome: sugar versus sugar. Chem Mater. 2024;36:2420–31.
62. Wang J, Wang Z, Yu J, Kahkoska AR, Buse JB, Gu Z. Glucose-responsive insulin and delivery systems: innovation and translation. Adv Mater. 2020;32:1902004.

63. Walther M, Vestweber PK, Kühn S, Rieger U, Schäfer J, Münch C, Vogel-Kindgen S, Planz V, Windbergs M. Bioactive insulin-loaded electrospun wound dressings for localized drug delivery and stimulation of protein expression associated with wound healing. Mol Pharm. 2022;20:241–54.
64. Macedo AS, Mendes F, Filipe P, Reis S, Fonte P. Nanocarrier-mediated topical insulin delivery for wound healing. Materials. 2021;14:22.
65. Feng Q, Li D, Li Q, Cao X, Dong H. Microgel assembly: Fabrication, characteristics and application in tissue engineering and regenerative medicine. Bioactive materials. 2022;9:105–19.
66. Muir VG, Qazi TH, Weintraub S, Torres Maldonado BO, Arratia PE, Burdick JA. Sticking together: injectable granular hydrogels with increased functionality via dynamic covalent inter-particle crosslinking. Small. 2022;18:2201115.
67. Roy B, Palaniyandi SS. Tissue-specific role and associated downstream signaling pathways of adiponectin. Cell Biosci. 2021;11:18.
68. Heydarpour F, Sajadimajd S, Mirzarazi E, Haratipour P, Joshi T, Farzaei MH, Khan H, Echeverría J. Involvement of TGF-β and autophagy pathways in pathogenesis of diabetes: a comprehensive review on biological and pharmacological insights. Front Pharmacol. 2020;11:21.
69. Abdalla MMI. Therapeutic potential of adiponectin in prediabetes: strategies, challenges, and future directions. Ther Adv Endocrinol Metab. 2024;15:19.
70. Yan L, Jiang MY, Fan XS. Research into the anti-pulmonary fibrosis mechanism of Renshen Pingfei formula based on network pharmacology, metabolomics, and verification of AMPK/PPAR-γ pathway of active ingredients. J Ethnopharmacol. 2023;317:15.
71. Foretz M, Guigas B, Viollet B. Metformin: update on mechanisms of action and repurposing potential. Nat Rev Endocrinol. 2023;19:460–76.
72. Rodríguez C, Muñoz M, Contreras C, Prieto D. AMPK, metabolism, and vascular function. FEBS J. 2021;288:3746–71.
73. Yang X, Zhu SM, Li L, Zhang L, Xian S, Wang YQ, Cheng YX. Identification of differentially expressed genes and signaling pathways in ovarian cancer by integrated bioinformatics analysis. Onco Targets Ther. 2018;11:1457–74.
74. Kumar SU, Kumar DT, Bithia R, Sankar S, Magesh R, Sidenna M, Doss CGP, Zayed H. Analysis of differentially expressed genes and molecular pathways in familial hypercholesterolemia involved in atherosclerosis: a systematic and bioinformatics approach. Front Genet. 2020;11:16.
75. Han M, Liu Z, Xu YY, Liu XT, Wang DW, Li F, Wang Y, Bi JZ. Abnormality of m6A mRNA methylation is involved in Alzheimer's disease. Front Neurosci. 2020;14:9.
76. Liu HB, Chen R, Wang PK, Fu JL, Tang ZA, Xie JJ, Ning YH, Gao J, Zhong Q, Pan X, et al. Electrospun polyvinyl alcohol-chitosan dressing stimulates infected diabetic wound healing with combined reactive oxygen species scavenging and antibacterial abilities. Carbohyd Polym. 2023;316:15.
77. Namjoo M, Ghafouri H, Assareh E, Aref AR, Mostafavi E, Hamrahi Mohsen A, Balalaie S, Broussy S, Asghari SM. A VEGFB-based peptidomimetic inhibits VEGFR2-mediated PI3K/Akt/mTOR and PLCgamma/ERK signaling and elicits apoptotic, antiangiogenic, and antitumor activities. Pharmaceuticals (Basel, Switzerland). 2023;16:906.
78. Astinfeshan M, Rasmi Y, Kheradmand F, Karimipour M, Rahbarghazi R, Aramwit P, Nasirzadeh M, Daeihassani B, Shirpoor A, Gholinejad Z, Saboory E. Curcumin inhibits angiogenesis in endothelial cells using downregulation of the PI3K/Akt signaling pathway. Food Biosci. 2019;29:86–93.
79. Du FZ, Liu MM, Wang JW, Hu LZ, Zeng DA, Zhou SC, Zhang LX, Wang MJ, Xu X, Li CL, et al. Metformin coordinates with mesenchymal cells to promote VEGF-mediated angiogenesis in diabetic wound healing through Akt/mTOR activation. Metab-Clin Exp. 2023;140:15.
80. Tombulturk FK, Soydas T, Kanigur-Sultuybek G. Topical metformin accelerates wound healing by promoting collagen synthesis and inhibiting apoptosis in a diabetic wound model. Int Wound J. 2023;12:e14345.

Publisher's Note